Synthesis and Characterization of bulk and Nano sheets of 4d and 5d based layered Transition Metal Oxides

A Thesis

submitted to

Indian Institute of Science Education and Research Pune
in partial fulfillment of the requirements for the
BS-MS Dual Degree Programme

by

B Bharat Chand

Indian Institute of Science Education and Research Pune
Dr. Homi Bhabha Road,
Pashan, Pune 411008, INDIA.

May , 2019

Supervisor: Dr. Sunil Nair

Co-Supervisor: Dr Ashna Bajpai
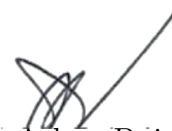
© B Bharat Chand   2019

Certificate

This is to certify that this dissertation entitled **Synthesis and Characterization of bulk and Nano sheets of 4d and 5d based layered Transition Metal Oxides** towards the partial fulfilment of the BS-MS dual degree programme at the Indian Institute of Science Education and Research, Pune represents study/work carried out by B Bharat Chand at Indian Institute of Science Education and Research under the supervision of Dr. Sunil Nair , Associate Professor , Department of Physics and co-supervision of Dr. Ashna Bajpai, Visiting Faculty, Department of Physics, during the academic year 2018-2019 .

Dr. Sunil Nair

Dr. Ashna Bajpai

Committee:

Dr. Sunil Nair

Dr. Ashna Bajpai

Dr. Mukul Kabir

This thesis is dedicated to my family and friends

Declaration

I hereby declare that the matter embodied in the report entitled **Synthesis and Characterization of bulk and Nano sheets of 4d and 5d based layered Transition Metal Oxides** , are the results of the work carried out by me at the Department of Physics , Indian Institute of Science Education and Research, Pune, under the supervision of Dr. Sunil Nair and co-supervision of Dr Ashna Bajpai and the same has not been submitted elsewhere for any other degree.

B Bharat Chand

Acknowledgments

I would like to thank my co-supervisor, Dr. Ashna Bajpai for her constant support, guidance and motivation during my time as her student. She helped me with all her patience to guide me in understanding a research problem and helped me tackle it. I am extremely grateful to have such a tremendous mentor. I would like to thank my supervisor Dr Sunil Nair for the advice and encouragement provided by him through out my entire project. I thank him for providing insightful discussions and suggestions regarding my research work .

I would like to thank my lab members, Namrata for helping me in synthesis techniques and for her kindness to help me in understanding softwares, Aakanksha for helping me in Rietveld analysis and helping me with all my queries, and Nitesh for interesting discussions off topic. I take this opportunity to thank Dr A.K.Nigam and Mr J.Paramar for TEM imaging of $SrRu_2O_6$. I take this opportunity to thank Dr Shivprasad Patil and his lab member Shatruhan Singh Rajput for helping me complete my AFM measurements. I would like to thank Shruti Chakravarthy for helping me in hydrothermal technique for doping $SrRu_2O_6$ and also for thermal diffusivity measurements. I thank Suvidya Homkar, previous year MS student for guiding me in liquid exfoliation technique. I thank Charu Garg for the Synchroton data measurements of my sample. I thank the technical staff in $\hbar$, Nilesh Dumbre, Anil Shetty, T.S.Yatish for their support. I thank all my friends for the wonderful time we had at IISER. I would like to thank IISER for giving me this platform to do research and DST for INSPIRE fellowship.

Finally, I must express my gratitude to my parents, sister and grandparents for providing me with continous support and unfailing encouragement throughout my years of study. This accomplishment would not have been possible without them.

x

List of Publications

1. Suvidyakumar Homkar, **B Bharat Chand**, Shatruhan Singh Rajput, Shivprasad Patil, Ruediger Klingeler, Sunil Nair, Ashna Bajpai. *Atomically thin sheets of the layered honeycomb magnet SrRu2O6 by liquid exfoliation.*[arXiv:1904.12326]

Abstract

4d and 5d transition metal oxides (TMOs) crystallising in a honeycomb lattice and comprising of magnetic ions with strong spin-orbit coupling provide new avenues for current research in the condensed matter. Such TMOs with layered quasi 2-dimensional structures are even more interesting. This is due to the fact that layered TMOs can lead to experimental realization of *graphene-like* nanosheets with magnetic honeycomb lattice. First part of this thesis deals with a new layered compound $Sr_xCa_{1-x}Ru_2O_6$, for which the parent $SrRu_2O_6$ has been theoretically predicted to exhibit topological states under strain. Here $SrRu_2O_6$ is a room temperature antiferromagnetic insulator and hence important for device applications based on topological materials. Thus doping in the parent compound as well as formation of graphene -like sheets of the doped compound are possible approaches to tune the strain. The doped sample has been successfully synthesized by Hydrothermal route and characterized through Rietveld Profile Refinement of synchrotron X-ray diffraction (XRD) data. The results of structural analysis reveal a clear anomaly in the lattice parameters near the room temperature. We have also conducted thermal diffusivity measurements on the pressed pellet of the parent and the doped $SrRu_2O_6$, which confirm the possibility of change in thermal properties near the room temperature. Further to this, $Sr_xCa_{1-x}Ru_2O_6$ in the form of nanosheets has been obtained using the technique of liquid exfoliation. These atomically thin nanosheets of parent as well as doped compound have been characterized through Transmission Electron Microscopy (TEM) and Atomic Force Microscopy (AFM). In the second part of the thesis, the nanosheets of two Kitaev magnets Na_2IrO_3 and $RuCl_3$ have been further characterized through TEM and AFM.

Contents

List of Figures

List of Tables

3

Chapter 1

Introduction

1.1 Transition Metal Oxides

Transition metal oxides have attracted the interest of the scientific society since a long time, dating back to the Greek era when a peculiar mineral Fe_2O_3(Hematite) showed amazing magnetic properties. The study of 3d magnetic oxides even continued through the 19th century and till the late 20th century with much attention given to the magnetic and electronic properties of the oxides. The interest was rekindled during 1986 when the cuprate family of the Transition metal oxides(TMO's) was reported to exhibit high-temperature superconductivity. Being magnetic materials, 3d TMO's are valuable not only as magnets but also as electronic materials. The study of electronic properties of 3d TMO's helped in the production of active materials in transistors which expanded this field greatly studying various aspects of TMO transistors[3]. Then the manganite family has attracted attention with very high values of magnetoresistance. Thus the 3d TMO's branched into diverse fields varying from the pursuit of high-temperature superconductors to Colossal Magnetoresistance[1]. Hence the transition metal oxides, in general, have been the topic of intense study for experimental as well as theoretical condensed matter physics.

As the study advances to 4d and 5d TMO's, the physics remarkably changed from the 3d TMO's. Along with the strong correlations, there exists a considerable amount of Spin-orbit coupling in 4d and 5d TMO's. This gives rise to some exotic phenomena

like topological insulators and semiconductors [4]. Hence 4d and 5d TMO have become popular areas of research in condensed matter physics with many unanswered questions. In this thesis, we have primarily investigated some 4d and 5d based TMOs with a layered structure. The purpose of investigating these compounds, along with the parameters relevant to this study have been explained in the sections ahead.

1.2   Layered Transition Metal Oxides

Layered transition metal oxides (TMOs) with quasi 2-dimensional structure and weak interlayer coupling can be exfoliated in the form of graphene-like sheets[42]. The discovery of graphene (layers of graphite) revolutionized industry as well as academia in many ways. Graphene has very interesting characteristics like high mechanical strength, high electrical and thermal conductivity, high surface area and electron mobility[17-20]. Thus graphene became an excellent material for various applications like sensor devices, energy storage, and conversion devices [21,22]. It has been thoroughly and extensively studied that other materials were explored to find such properties. The exotic properties of graphene are derived from the honeycomb lattice of carbon atoms that gives rise to linear dispersion in band structure and the low energy excitations of massless Fermions. However, carbon being a light atom, this system has small spin orbit coupling. The systems discussed in this project form magnetic honeycomb lattice comprising of heavy ions such as Ru and Ir. The layered transition metal oxides, especially with magnetic honeycomb lattice can become the next important topic of research for applications as well as rich physical phenomena exhibited by them. Delamination of the layered compounds has the potential to change the physics understood from their 3D bulk counterpart. The resulting individual layers are often referred to as nanosheets due to their 2D morphology[11,12]. Oxide nanosheets are extremely promising due to their structural, electronic and magnetic properties and their potential applications in nanoelectronics and catalysis [13-16]. We first discuss some general properties of Transition metal oxides and explain the relevant terms, particularly in context of their exotic magnetic and electronic properties.

In 3d based TMOs , the important parameters that are needed to explain metal insulator transition, Superconducting transition and collosal magnetoresistance etc.

are correlation parameter (U), bandwidth (W), Spin-Orbit Coupling (SOC) which is generally small and this term can be ignored in 3d oxides. However for 4d and 5d systems SOC is an important and crucial parameter. in the following we explain each of these parameters.

In order to explain such novel phenomena associated with these topological states, we have to understand the interplay of bandwidth(W), Coulomb correlation(U) and spin-orbit coupling(λ) which are explained in the next section.

1.3 Transition Metal Oxides : Theoretical Background

In order to answer the question whether a solid is a metal or an insulator, the first theory that was introduced was free electron theory by Paul Drude which used classical statistics to explain properties of solids. The electronic properties of metals could be explained but the theory failed to explain thermodynamic properties of metals. Sommerfeld modified this theory using the Pauli exclusion principle and considering the electron in a bound state. Thermodynamic properties of metals could be explained by this model when metals are assumed as non-interacting Fermi gas. However, this model failed to explain insulators because in this model electrons could move freely around positive metal ions. After the advance of X-ray Crystallography, it was observed that molecules in a solid are arranged periodically. Different types of periodic arrangements were observed and all were classified into different Bravais lattices. Now, electrons in a crystalline solid experience a periodic potential, because all the metal nuclei sit in a lattice. Since there is periodicity in potential, it can be written mathematically as

$$U(\mathbf{r} + \mathbf{R}) = U(\mathbf{r}) \tag{1.1}$$

where $\mathbf{R}$ is a Bravais lattice vector. Now electrons motion can be solved by using Schrodinger's equation for this potential. Using the famous Bloch's theorem the wave function was determined by the fact that potential is periodic.

$$\psi_{n\mathbf{k}}(\mathbf{r}) = e^{(i\mathbf{k}.\mathbf{r})} U_{n\mathbf{k}}(\mathbf{r}) \tag{1.2}$$

$$U_{n\mathbf{k}}(\mathbf{r} + \mathbf{R}) = U_{n\mathbf{k}}(\mathbf{r}) \tag{1.3}$$

where n is band index, $\mathbf{k}$ is the wave vector. Many metals could be explained using the above wave function. However, Tight-binding model could explain metals as well as different insulators. This model considers the orbitals of nearest neighbouring atoms to be overlapped over each other and then the wave function is determined using weak interactions of neighbouring atoms [6]. Further Hartree Fock considered even the electron-electron repulsion by averaging the field of all other electrons for a single electron in a particular site. Though this approach could tackle the problem of many-body system, some experimental findings showed deviations. Since the band theory could not explain CoO insulating properties [5], there should be a better way to understand periodic potential and interactions between electrons. In order to solve this problem, a new method was introduced where the interactions between electrons were treated differently. This model was derived by Hubbard, Gutzwiller, and Kanamori which changed the physics of correlated electron systems.

In TMO's the 4d or 5d metal ions are surrounded by O^{2-} anions via covalent bonding. Transition metal ions have valence electrons in d orbital hence they are also called d electron system. All the d-orbitals in an isolated transition metal ion are always degenerate. In a solid containing only TM ions, the overlap of neighbouring atoms d orbitals is less as the spatial extension of a d orbital in a TM ion is less. Hence the bandwidth(W) of TM is less compared to an alkaline metal[7].

1.3.1   Crystal Field

In TMO's the metal ion is surrounded by oxygen ligands in different geometries. The orbitals of the O^{2-} ions overlap with the orbitals of TM ion which eliminates the degeneracy of the d orbitals in a TM ion. The d-orbitals $d_{xy}, d_{yz}, d_{xz}, d_{x^2-y^2}$, $d_{3z^2-r^2}$ no longer have the same energy. Depending on the geometry of O^{2-} ions, generally in a TMO, the O^{2-} ions are octahedrally arranged around a TM ion equidistantly. Since the O^{2-} ligand has negative field and arranged in an octahedral configuration there is electrostatic repulsion only in the x,y,z direction. Under this crystal field the $d_{x^2-y^2}$ and $d_{3z^2-r^2}$ shift to higher energy e_g state , while the d_{xy}, d_{yz}, d_{xz} shift to lower energy t_2g state. This difference in energy of the t_2g and e_g state is called the crystal

field splitting which is 10 Dq for TMO's that is approximately 2-3 eV. In some cases the octahedron distorts along any of the cubic axis(x,y,z) which leads to tetragonal distortion, for example, John Teller distortion in 3d TMO's[8].

1.3.2   Spin-Orbit Coupling (λ)

The electronic state of a solid is determined by cosidering the electron in a single site. The 4d and 5d metal oxides contains heavy nuclei with electrons that have considerable Orbital angular momentum (**L**) and Spin Angular momentum (**S**). The interaction between **L** and **S** of an electron determines the electronic state in a solid, so the spin-orbit Hamiltonian is

$$H_{SO} = \lambda \mathbf{L}.\mathbf{S} \tag{1.4}$$

The expectation value of this Hamiltonian acting on one electron wave function gives λ as Eigen value($<\psi|H_{SO}|\psi> = \lambda$). The Spin-orbit coupling (λ) goes as Z^4 in high atomic number elements[7].

1.3.3   Hubbard model

The Hubbard model considers electron-electron interaction in the periodic lattice as many-body problem. This model when applied on simple electron systems which are non-relativistic have a simple Hamiltonian which is,

$$H = \sum_i \frac{(P_i)^2}{2m} + \sum_i V(\vec{r_i}) + \frac{1}{2} \sum_{i \neq j} U(\vec{r_i}, \vec{r_j}) \tag{1.5}$$

where i is sum over all electrons. The first term is the kinetic energy of the electron, the second term is the potential from the nuclei, for simplicity the motion of the nuclei is not taken into account. The third term is electron-electron interaction which is $U(\vec{r_i}, \vec{r_j}) = \frac{e^2}{|\vec{r_i} - \vec{r_j}|}$. Though the equation appears simple it can not solve the many-electron system unless we use certain approximations. In a TM ion, the core electrons are tightly bound to the nuclei and effectively screened compared to valence electrons. Hence only Valence electrons of TM ion is considered to solve this problem. This

approach effectively converts the Hamiltonian into a complex form which can be written as $H = H_{tb} + H_U$. The first term is effectively the kinetic energy or tight binding term which contains the coefficient t which is the hopping amplitude. The second term is the Coulomb energy term which contains the coefficient Coulomb interaction (U). In the finite limit when $(U < t)$, electron hopping is possible and the system attains a metallic state. In the case of $(U > t$), the electron is localized in a single site and is not free to move in the lattice, hence the system attains an insulating state[9].

In TMO's as we go from 3d to 5d oxides, the spatial extension of d-orbital increases for the TM ion, hence the Bandwinth(W) of the TMO increases down the group. We know the relation between Spin-orbit coupling (λ) and atomic number (λ α Z^4), hence (λ) increases down the periodic table. The Coulumb interaction (U) is inversely proportional to the distance between two interacting electrons. Hence TMO's with smaller bandwidth has higher Coulumb interaction value and reduces as we go to 5d oxides. [Fig 1.1 (a)] clearly shows which exotic phenomena is exhibited by the materials based on the variation of (U) and (λ). We observe that in the regime of weak correlations we find topological band insulators. As U and λ increases we find spin orbit assisted mott insulator states arising after the metal band insulator states in materials. However when Spin-orbit coupling becomes significant we observe bond directional exchange interactions in materials. This ultimately leads to unusual types of magnetism in materials like the emergence of spin liquid states. These materials became popular as the Kitaev materials. As these exotic states can be realised from the exactly solvable Kitaev model on materials with Honeycomb lattice structure[30].

1.3.4   Kitaev model and Honeycomb Lattice

In a honeycomb lattice with spin $\frac{1}{2}$ sitting on each of the lattice points, there are three different links through which the nearest neighbouring spins interact in different ways. The different ways are x-,y- and z- interaction which can be described using Pauli spin operators σ_i^α where α =x,y,z and is used for indexing the site . The Hamiltonian

for this system can be written as

$$H = -j_x \sum_{x-links} \sigma_j^x \sigma_k^x + -j_y \sum_{y-links} \sigma_j^y \sigma_k^y + -j_z \sum_{z-links} \sigma_j^z \sigma_k^z \qquad (1.6)$$

where j_x, j_y and j_z are exchange coupling constants. Na_2IrO_3, Li_2IrO_3 and $RuCl_3$ were the first candidates to realize Kitaev model in their Honeycomb lattice [10]. Thus the Kitaev materials got increased attention in experimental as well as theoretical condensed matter fields.

1.4 Some 4d and 5d based TMOs with Magnetic Honeycomb Structure

1.4.1 $SrRu_2O_6$ and $Sr_xCa_{1-x}Ru_2O_6$

$SrRu_2O_6$ has a quasi 2-Dimensional structure and is a high-temperature antiferromagnet with a Neel temperature, $T_N = 565K$[25]. It has P$\bar{3}$1m space group with lattice parameters as a=5.20573$\overset{\circ}{A}$, c=5.23454 $\overset{\circ}{A}$[23]. The edge sharing RuO_6 octahedra forming a honeycomb lattice are alternately stacked with an intervening layer or Sr cations that are octahedrally coordinated.[Fig 1.1 (b)] shows the geometrical structure of $SrRu_2O_6$. Experimental studies show that at room temperature there is antiferromagnetic order in the a-b plane as well as along the c direction in the crystal lattice. It was predicted that via doping the A sites of the oxide the antiferromagnetic order may be destroyed, and the possibility of change in magnetic properties, due to the layered structure of the compound, and also the possibility of tuning thermal properties [24]. Under this assumption, my project involves the doping of the parent compound $SrRu_2O_6$ with a stoichiometric proportion of 10% Calcium and 30% Calcium.

$Sr_xCa_{1-x}Ru_2O_6$ is a new compound that was synthesized by modifying the parameters of parent compound reported by C.I.Hiley and group [23].It shares the same structure as the parent compound. The edge-sharing octahedra forms a honeycomb lattice in the a-b plane. Alternate layers containing Ca ions and Sr ions are stacked
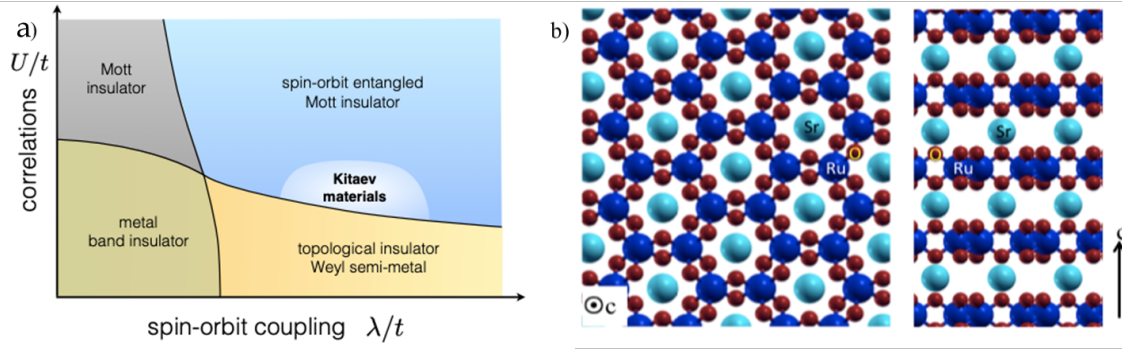
Figure 1.1: [23,7] a)Illustration of phase Diagram in the presence of electron correlations and spin orbit coupling b) Geometric structure of $SrRu_2O_6$ when viewed along the c axis and perpendicular to the c axis.Here light blue,dark blue and small black balls are Sr,Ru and O atoms respectively

between the RuO_6 octahedra. It has been reported that this non-centrosymmetric oxide has the possibility of exhibiting excellent metallicity. Density Functional Calculations on the parent compound have predicted strain mediated topological properties and hence the approach of (i) doping the parent compound as well as (ii) formation of graphene like 2-D sheets of the doped version can provide experimental realization of these predictions[26].

1.4.2 Na_2IrO_3 and $RuCl_3$

When we look into the crystal structure of Na_2IrO_3 [Fig 1.2 (a)], it consists of alternating layers of $NaIr_2O_6$ stacked with an intervening layer of Na atoms. The $NaIr_2O_6$ layers contains edge sharing IrO_6 octahedra and the Na atoms occupy the voids in the octahedra. If we view from the c axis we find the IrO_6 octahedra forms a honeycomb lattice in the a-b plane. Theoretically it was explained that the interactions of Spin 1/2 elements sitting on a honeycomb lattice follows a Kitaev-Heisenberg model[27], which induces quantum spin liquid ground states. In contradiction it was experimentally shown that Na_2IrO_3 has a long range antiferromagnetic ordering in 3- dimension in zig zag order below the Neel temperature $T_N = 13.3$ K [28].

Similar to Na_2IrO_3 crystal structure $RuCl_3$ also have edge sharing $RuCl_6$ octahedra forming a honeycomb lattice in the a-b plane which in turn are stacked one above
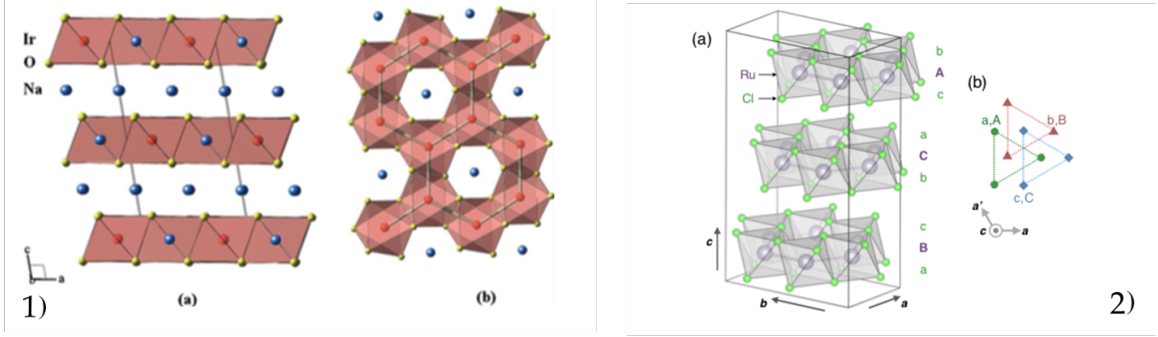
Figure 1.2: [28,29] (1)Geometric structure of Na_2IrO_3 as viewed perpendicular to c axis and along the a-b plane. Here blue,orange and yellow colored balls are Na,Ir and O atoms respectively (2) Geometric structure of $RuCl_3$. Here grey and yellow balls are Ru and Cl atoms respectively

the other in c direction. However, the Cl-Ru-Cl bond angle in the case of $RuCl_3$ is 90° while the O-Ir-O bond angle is 85° [29]. Geometrical structure of $RuCl_3$ is shown in [fig 1.2 (b)]. Another structural difference is the absence of the intervening Na atoms between the honeycomb layers which makes $RuCl_3$ an ideal 2- Dimensional system. Another difference between Na_2IrO_3 and $RuCl_3$ is the large size of Cl anions, this actually expands the lattice. Recent experimental studies explored the possibility of destroying the long-range ordering in $RuCl_3$ by delaminating the layered structure to a few layers of nanosheets. It also investigated the possibility of tuning the Kitaev paramagnetic state in $RuCl_3$ via exfoliation [31]. The compounds have been exfoliated using liquid exfoliation technique and the characterization of their respective exfoliated sheets by AFM has been done during my project.

1.5 Plan of Thesis

Various properties of TMO materials can be tuned like electronic or magnetic just by varying temperature, pressure or by doping the TMO. In the first part of the thesis, we aim to dope $SrRu_2O_6$ with Ca metal ion. Then we characterize the doped compound using microscopy and diffraction techniques. Followed by Rietveld Analysis of synchrotron diffraction data. We have also performed thermal conductivity and transport measurements on both the samples , parent as well as doped compound.

Further, the doped compund has also been exfoliated and characterized. The second part of the thesis involves studying the 2d layered TMO's with Honeycomb Lattice. Na_2IrO_3 and $RuCl_3$. These two TMO's have been successfully exfoliated and the characterisation of these exfoliated nanosheets are presented

Chapter 2

Methods and Techniques of characterization

2.1 Methods

2.1.1 Hydrothermal technique

Hydrothermal synthesis is a critically acclaimed technique in the materials science field and Solid state physics. It has served various important purposes like crystal growth and synthesis of new functional materials with useful properties[35]. Basically, it is a chemical reaction in the presence of aqueous solvents at temperatures greater than 100° and pressures greater than 1 atm in a closed system like a Teflon cup. However, the teflon cup is contained in a metallic container to withstand the extreme pressure and temperature conditions. The high pressure helps to dissolve or recrystallize materials which are relatively insoluble in normal conditions. Hydrothermal synthesis generally has a wide range of applications which include synthesizing single crystals, doping and stabilizing new functional materials, producing Zeolites and other microporous substances. Finely divided material can be prepared with microcrystallites. Further the morphology and size of the microcrystallites can be controlled
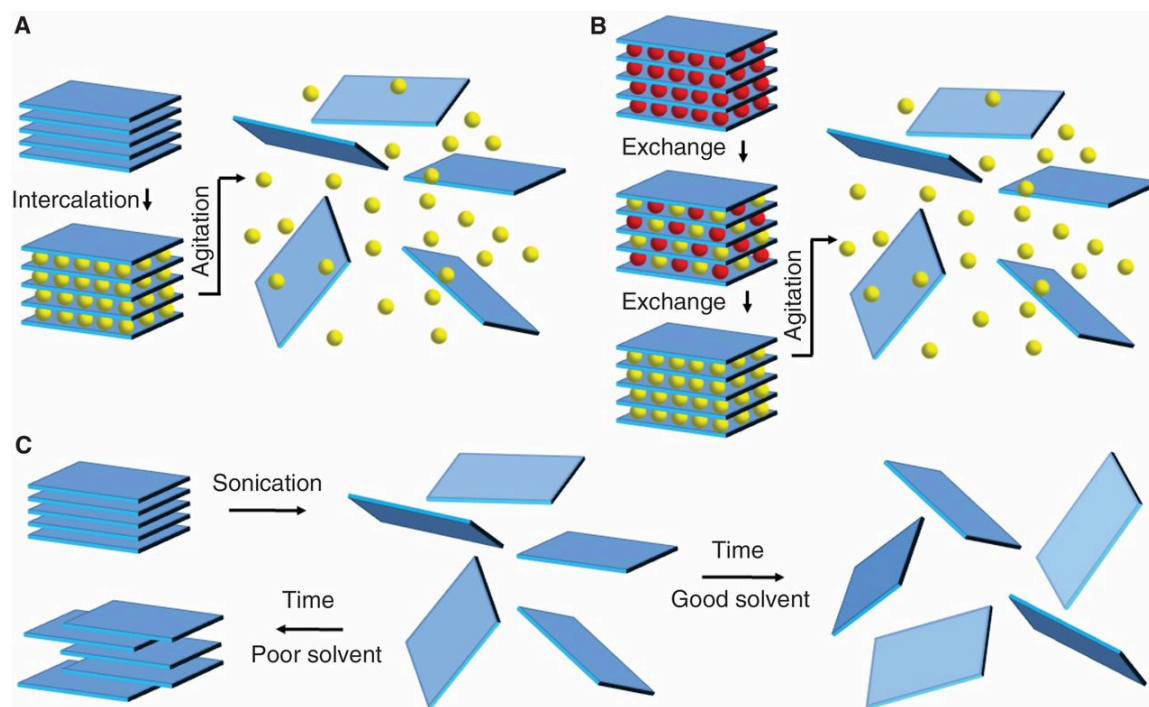
Figure 2.1: [33] The Schematic of liquid exfoliation using (a)ion intercalation (b)ion-exchange and (c) good solvent

2.1.2   Liquid Exfoliation Technique

Graphene can be mechanically exfoliated from a piece of graphite by scotch tape attaining 1 atom thick graphene sheets (Geim and Novoselov et.al)(42). A lot of materials including chalcogenides which possess Van der Waals bonds can be exfoliated in this manner. However, a scalable technique is required if devices are to be fabricated using atomically thin 2-D sheets. This was achieved by the technique of liquid exfoliation by (Nicolosi and coleman et.al) who demonstrated a successful and scalable technique to obtain such nano sheets [33]. Though the TMO's we discussed in this project are quasi 2-D but they are not Vander Waals driven. However, we successfully employed this technique to obtain nano sheets of $SrRu_2O_6$, Na_2IrO_3, $RuCl_3$ in our lab (43). This technique is discussed in detail in the following.

The liquid exfoliation process involves finding a suitable liquid medium in which the compound to be exfoliated can be sonicated. The process of sonication leads to breaking of the individual layers through the weaker bonds, which are responsible

for the inherent layered structure. The sonication step is followed by centrifugation that enables selection of individual layers according to thickness, by the formation of density gradient. The centrifuged solution is carefully stored without any mechanical vibrations so as to avoid mixing of density separated layers. This simple process enables the formation of monolayers as well as few atomically layer thick sheets according to the need. The main experimental parameters are (i) proper choice of liquid solvent, that prevents coagulation of the separated layers post sonication (ii) sonication time and centrifuge time. These parameters need to be optimized.

2.2 Microscopy Techniques

2.2.1 Scanning Electron Microscopy(SEM)

SEM is the preliminary and important characterization tool to study any functional material in nanoscience. It is used to get information about the 3-d morphology,size, and shape of the sample. During imaging, a beam of high energy electrons are focussed at a fine point on the specimen and raster scans are performed on an area in the range of microns. When the electron beam hits the sample it scatters elastically and inelastically from the specimen at varying depths resulting in different types of signals. These signals are classified as secondary electrons (SE), Auger electrons and Backscattered electrons (BSE), Bremsstrahlung X-rays which gives a variety of information about the specimen. The SE's are due to inelastic interactions with the sample at the surface region and provide detailed information about the surface of the sample. The BSE's are due to inelastic interactions and originate from a much deeper region. They are sensitive to atomic number and give much brighter images for higher atomic number sample. ZEISS ultra plus is the instrument used for sample analysis in this project.W/ZrO cathode is used for electron emission and the energy range of emitted electrons is (3 KeV- 30KeV). All the images taken are either in In-Lens or SE2 mode. Inlens mode is used for higher resolution while SE2 mode is used for higher contrast. It should be kept in mind that unlike optical microscopy, there can be damage to the sample by high energy electrons in electron microscopy.

This instrument also has the option for Energy Dispersive analysis of Spectroscopy
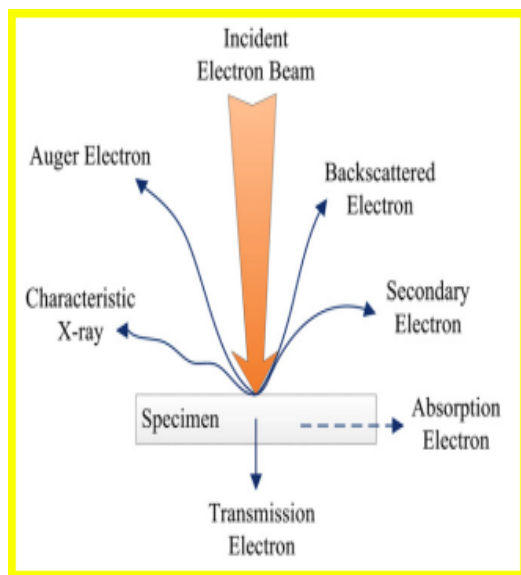
Figure 2.2: [36]Different signals emitted when electron beam hits the sample surface

(EDAX). It is used to find the elemental composition of the sample. When the electron hits the sample X-rays are emitted from sample respective to the elements present in the sample. This spectrum is recorded in a detector and the atomic percentage of the elements present in the sample is calculated. The advantage of this technique is that it is non-destructive to the sample.

2.2.2   Transmission Electron Microscopy (TEM)

In TEM a broad beam of electrons passes through an ultra-thin specimen, the transmitted electrons form an image on the fluorescent screen. TEM uses (LaB_6) source which generates much higher energy electrons in the range (60 KeV - 400 KeV). Hence provides much better resolution of 0.2 nm while the SEM is restricted to a resolution of 2 nm. The specimen used should be less than 100 nm, so usually, a suspension of the sample is drop-casted on a TEM grid for imaging. Apart from imaging, TEM also provides structural and crystallographic information. There are two ways of recording diffraction measurement on TEM. First, one using an objective aperture only recoding diffracted beams of a certain area. Secondly, the beam can be directed to the targeted area where the diffraction is observed. There are also a few disadvantages of using TEM, firstly there is a higher chance of sample damage. Secondly, the volume
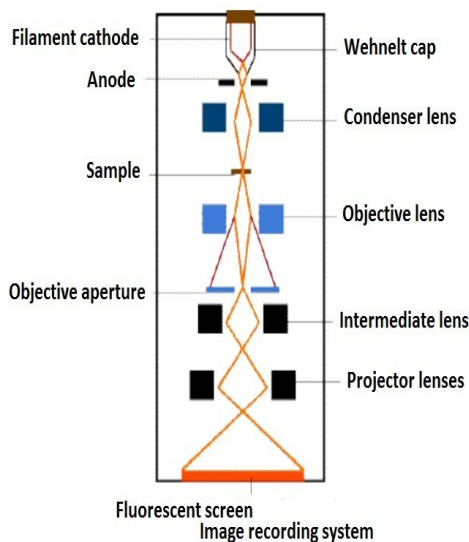
Figure 2.3: [37] The Schematic of the TEM Instrument

of the sample analysed is very low so the sample should be imaged first on a larger scale in a low resolution instrument. Jeol JEM 2200 FS is used in this project It has an acceleration voltage of 200 KeV

2.2.3   Atomic force Microscopy(AFM)

AFM is extensively used in nanoscience for specific topographical information like the height of the sample apart from other morphological information. The basic ingredients of AFM instrument is good cantilever tip assembly, an optical detection method using a laser beam and a feedback loop controlled by tip-sample interaction forces. For imaging a sample AFM uses a cantilever with a sharp tip and raster scans a micron-sized area of the sample. When the tip approaches the sample, there is either a repulsive or attractive force between the tip and sample. This force deflects the cantilever which is recorded in the detector using a laser beam incident on the cantilever-tip assembly. The deflection is kept constant using a feedback loop and moving the sample towards or away from the tip. A constant force gradient is attained across the sample using this controlled movement. The sample holder is finely controlled using piezoelectric materials.
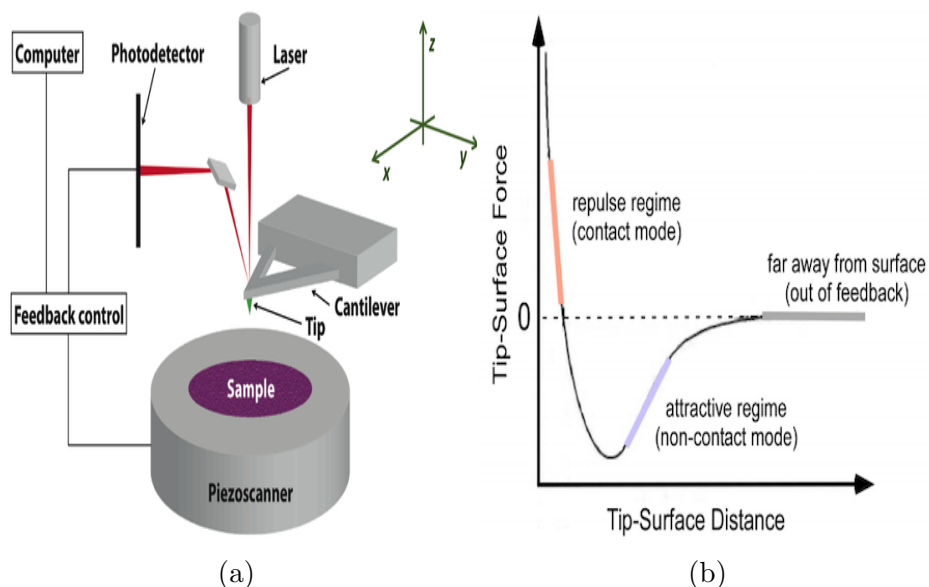
Figure 2.4: [38] (a) The Schematic diagram of AFM , (b)Illustration of tip-sample interaction force in different modes

There are two general working modes in AFM which are contact and non-contact mode. In Contact mode, the deflection of the cantilever is kept constant. In the non-contact mode, the tip is vibrated at a constant frequency over the sample and amplitude is kept constant. In this project, JPK Nanowizard 2, is used for sample analysis. It has Silicon Nitride (Si_3N_4) cantilever with stiffness of 0.05 nm and the tip radius is 10 nm. All the imaging is done in contact mode using mica as the substrate. Since illumination is not used in AFM, the resolution of AFM is not controlled by the wavelength of light or aberration of the lenses. The resolution of the AFM is determined by the tip-diameter and separation between the tip-sample, it basically reaches up to atomic resolution if a very fine tip is used. The distinctive features of AFM from the electron microscopy is that it provides information in vertical i.e in the z dimension (if the sample is in the x-y plane) and non-conductive samples can also be imaged in AFM.
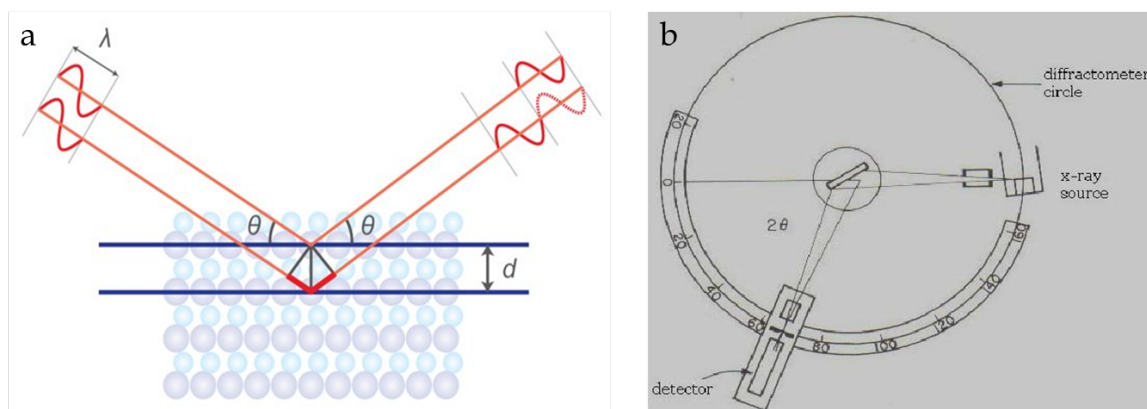
Figure 2.5: [39] (a) Phenomena of diffraction across the atomic planes , (b) The schematic of the phenomena in diffractometer

2.3 Diffraction Techniques

2.3.1 Powder X-ray Diffraction

X-ray diffraction is an analytical technique used for identifying different phases in a crystalline sample. It also gives information about the degree of crystallinity, unit cell parameters and atomic spacings of the sample. In the diffractometer, X-rays are generated when electrons hit the copper anode and Ni filter is used to focus monochromatic X-rays on to the sample. The crystalline powder sample contains differently sized crystallites oriented in a different direction. When X-rays hit the sample they get diffracted along the different planes of the crystalline sample and interferes either constructively or destructively. Constructive Interference of the X-rays is recorded in the detector, the angle at which this interference occurs is determined by the Bragg's Law.

$$n\lambda = d_{hkl}sin\theta \tag{2.1}$$

When the X-ray source is at an angle θ to the sample, the detector mounted on the arm moves in a circle such that it is 2θ from the sample. We get the final 2θ values where the intensity of reflections are strong. Bruker D8 Advance is used to characterize all the samples. It has Cu target with $k_{\alpha1}$=1.54 Å

2.3.2   Synchroton X-ray diffraction

The Basic principle in Synchrotron X-ray diffraction (XRD) is similar to the lab XRD. The X-rays get diffracted on the sample and the intensity of the Bragg reflections are detected. It basically differs from the lab XRD in four different aspects. It has the choice of using white radiation along with the option of monochromatic radiation. It gives us the freedom of using any wavelength from the available X-ray spectrum. Even after rejecting most of the incoming beam, the monochromatic beam is sufficiently intense and parallel[40]. The X-ray beam generated is comparatively much intense than the lab diffractometer which gives a higher speed of recording the data and also good statistics. The monochromatic beam generated in lab XRD is actually spread over a larger range compared to the synchrotron beam which is an intense fine beam provides a much better resolution of the data acquired. In this project, the sample is analysed using 3rd generation Synchrotron system:PETRA(III) present in Hamburg, Germany. This instrument has 17 beamlines. P02.1 is the beamline used for aquiring the diffraction data of powder sample using a monochromatic radiation of wavelength (λ=0.20709$\mathring{A}$)

2.4   Rietveld refinement

Rietveld refinement is a very important and powerful technique to extract crystal structure information which is widely used in nanoscience. It is used for structural analysis of powder XRD data. The synthesis techniques are generally much difficult for growing single crystals than powder crystalline form. Hence Rietveld analysis became popular in materials science to get more information from the powder diffraction data. However, a good structural model is prerequisite for pattern fitting. The principle of Rietveld refinement is that if we know the physical properties of the incident X-rays and that of crystal, we can approximately calculate the diffraction pattern for the crystalline sample. Then the difference between the calculated pattern along with the background and the observed diffraction pattern is minimized by employing the non linear least squares method[34]. Mathematically it is represented

as minimising the function, which is weighted sum of squared differences as follows,

$$WSS = \sum_i w_i(I_i^{obs} - I_i^{calc})^2 \tag{2.2}$$

where i runs over all the 2θ points detected in the diffraction data and the weight $w_i = \frac{1}{I_i^{obs}}$. It is a nonlinear least squares fitting, with different parameters refined at each iteration[34]. The Intensity of the diffraction pattern can be calculated as follows

$$I_i^{calc} = S \sum_K L_K |F_K|^2 \phi(2\theta_i - 2\theta_K) P_K A + I_i^{bg} \tag{2.3}$$

where K runs over all the bragg planes(hkl) of the crystalline compound, S = Scale factor, L_K = Lorentz Polarization factor, ϕ = Bragg reflection profile function, A = Absorption factor, F_K = Structure Factor,P_K is the preferred Orientation and I_i^{bg} is the background intensity. The calculated pattern is then fitted with the observed pattern using software. Fullprof software is used in this project for the Rietveld refinement of the diffraction data. In order to judge the quality of fitting statistical parameters(or R-factors) are used which helps to gauge the goodness of a fit. The parameters weighted profile R-factor (R_{wp}^2), expected R-factor (R_{exp}^2) and Goodness of fit or Chi-squared value (χ^2) are defined as follows,

$$R_{wp}^2 = \frac{\sum_i w_i(I_i^{calc} - I_i^{obs})^2}{\sum_i w_i(I_i^{obs})^2} \tag{2.4}$$

$$R_{exp}^2 = \frac{N}{\sum_i w_i(I_i^{obs})^2} \tag{2.5}$$

$$\chi^2 = \frac{1}{N} \sum_i w_i(I_i^{calc} - I_i^{obs})^2 = \frac{R_{wp}^2}{R_{exp}^2} \tag{2.6}$$

Here N is the Number of data points in the diffraction data minus the number of parameters varied during the fitting. We have to keep in mind that for a correct Rietveld fit the Chi-squared value (χ^2) value should never be less than one but very close to one[45].

2.5   Thermal diffusivity measurements(LFA)

In order to calculate the thermal conductivity of our compounds we measure the thermal diffusivity values. The Laser Flash method is used to analyse the thermal diffusivity of the compound. It is measured using LFA - Linseis 1000 model in this project. This intrument uses an energy pulse(laser) which heats one side of a pelletised sample. The temperature of the backside of the pellet gradually rises with time due to the energy input from the front side[46]. There is a time dependance relation for this rise of temperature. Larger the thermal diffusivity of the sample, faster the heat energy reaches the backside. Thus we obtain thermal diffusivity value for a particular temperature. Then the sample is heated to different temperatures in the furnace .The furnace is maintained at constant temperature when the measurement of the thermal diffusivity is taken.

2.6   PPMS and Linkam THMS600 stage

The PPMS is an automated low-temperature and magnet system, for the measurement of material properties like specific heat, magnetic AC and DC susceptibility and both electrical and thermal transport properties like Hall Effect, thermoelectric figure of merit and Seebeck Effect.The temperature can be varied continuously between 1.9 K and 400 K, while a magnetic field of up to 16 Tesla can be applied. In this project,PPMS Evercool 2 with quantum design is used, DC resistivity measurements were done by varying temperature from 300K to 5K.

Linkam's THMS600 stage is used in this Project. It is used in many applications where physical measurements are required while heating/cooling of sample. They are particulary used where high heating/coooling rates and high level accuracy and stability are needed. It has a temperature range of -196°C to 600°C. Samples are quickly characterised by heating to within a few degrees of the required temperature and then stabilised there for required amount of time for accurate observations. The entire experiment can be saved as real time plot, exported for further analysis.

Chapter 3

Structural,Transport and thermal study of doped TMO

3.1   Synthesis of $Sr_xCa_{1-x}Ru_2O_6$

Doping of the layered TMO $SrRu_2O_6$ has been done using a hydrothermal technique. Synthesis of $SrRu_2O_6$ was reported in the literature[23], but the doping of the oxide has not been reported to the best of our knowledge. Hence the synthesis of the doped sample is backed up with required characterization techniques to convince that Calcium has actually replaced some part of the A-sites of the TMO. To dope the pure $SrRu_2O_6$, the original process was slightly modified with small changes in the parameters. The inorganic precursors Potassium ruthenate ($KRuO_4$), Strontium peroxide (SrO_2) and calcium oxide (CaO) were added in stoichiometric proportion in the required amount of distilled water. Stirring the mixture thoroughly to roughly attain a state of approximately uniform solution which is black in color. The mixture is contained in a Teflon cup, enclosed in autoclave and heated in an oven at a temperature of 200° for a duration of 24 hours. The Hydrothermal oven used in the doping process is from Parr instruments company. In the end, a black colored precipitate is found at the bottom of the Teflon cup and orange colored liquid at the top of the mixture. This liquid only contains RuO_2 phase hence it is discarded. The precipitate is vacuum filtered and washed with Acetone, distilled water, and dil HCl. In this project

three trials of synthesis were conducted where two involved 10% doping and the third trial for 30 % doping is done. The required amounts of the starting compounds and parameters followed are tabulated as follows

Table 3.1: Products required for doping

SNo	precursor	supplier	product-code
1	$KRuO_4$	Alfa Aesar	10378-50-4
2	SrO_2	Sigma aldrich	1314-18-7
3	CaO	Alfa Aesar	1305-78-8

Table 3.2: Concentrations required for doping

Trial No	$KRuO_4$ (milli-moles)	SrO_2 (milli-moles)	CaO (milli-moles)	doping-amount	Product obtained
1	3	1.35	0.15	10%	$Ca_{0.1}Sr_{0.9}Ru_2O_6$
2	3	1.35	0.15	10%	$Ca_{0.1}Sr_{0.9}Ru_2O_6$
3	3	1.05	0.45	30%	$Ca_{0.3}Sr_{0.7}Ru_2O_6$

3.2 Characterization of $Sr_xCa_{1-x}Ru_2O_6$

The SEM image of 10% doped sample ($Sr_{0.9}Ca_{0.1}Ru_2O_6$) is shown in the [fig 3.1]. We can observe that the powder sample contains crystallites of hexagonal shape. The size of the crystallites is in the range of $2\mu m$ - $4\mu m$. The highlighted area in the [fig 3.1 (a)] is zoomed in for its hexagonal shape. From [fig 3.1 (b)], we can see small particles dispersed on the hexagonal crystallites. These small particles are RuO_2 impurity. The SEM image of 30% doped sample ($Sr_{0.7}Ca_{0.3}Ru_2O_6$) is shown in [Fig 3.2 (a)]. The image does not show any hexagonal shapes but random and irregular shapes of varying size are seen. The zoomed in image further confirms the observation. Hence for both the Rietveld analysis and the thermal diffusivity measurements $Sr_{0.9}Ca_{0.1}Ru_2O_6$ is selected. Further EDAX measurements were done for both the compounds. The data shows that Sr:Ru atomic ratio for both the samples is approximately 1:2. Since lower atomic numbers are not accurately measured there is a low atomic percentage for the Ca atoms

XRD graph of $Sr_{0.9}Ca_{0.1}Ru_2O_6$(10% doping) and $Sr_{0.7}Ca_{0.3}Ru_2O_6$ (30% doping) are shown in the [fig 3.3]. The crystal structure of the doped compound remains
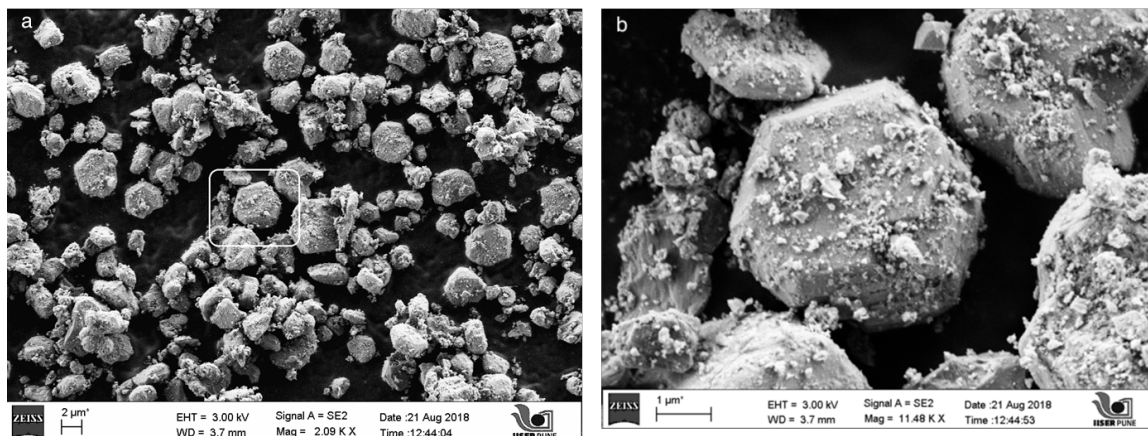
Figure 3.1: a)SEM image of $Sr_{0.9}Ca_{0.1}Ru_2O_6$ and b) magnified image of highlighted area

similar to the parent compound, $SrRu_2O_6$, as we are only trying to replace the A-sites of the parent compound. The Ca ions replace some of the Sr ions between the alternating layers of RuO_6 octahedra. The ionic radii of $Ca^{2+} = 114$pm while for $Sr^{2+} = 132$pm, this decrease in the ion size of the A-sites in the lattice structure affects the position of the Bragg peaks of the parent $SrRu_2O_6$. There is a systematic shift in the peak positions of the doped compound but the number of peaks obtained for both the compounds remains the same. The parent compound $SrRu_2O_6$ as reported previously by Suvidya et.al [43] also showed some peaks of RuO_2 phase. Similar

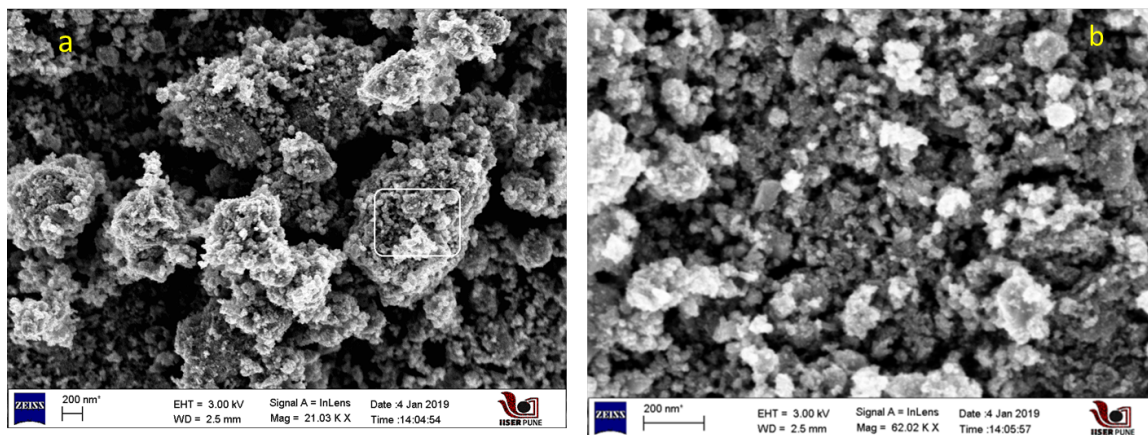

Figure 3.2: a)SEM image of $Sr_{0.7}Ca_{0.3}Ru_2O_6$ and b) magnified image of highlighted area
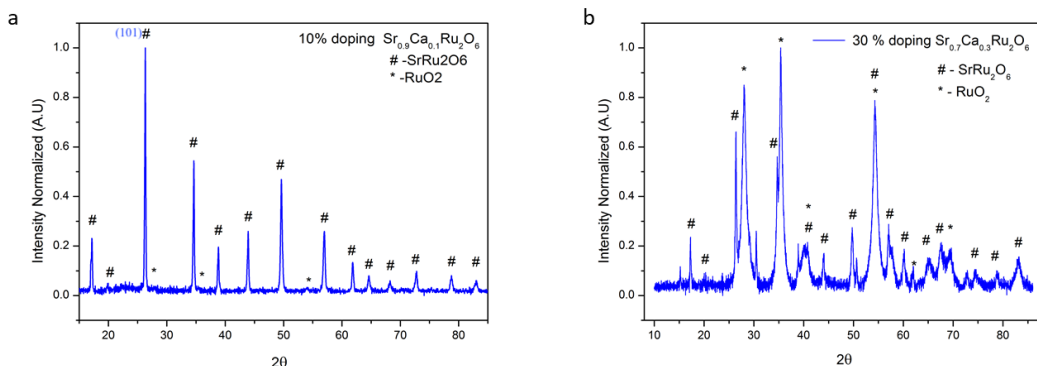
Figure 3.3: a)XRD graph of $Sr_{0.9}Ca_{0.1}Ru_2O_6$ and b) $Sr_{0.7}Ca_{0.3}Ru_2O_6$

result is expected for the doped compounds as both the compounds are synthesized following a similar experimental protocol. For the lab XRD data of both the doped compounds RuO_2 and $SrRu_2O_6$ peaks are indexed using the JCPDS data [99-500-2532] of RuO_2, [03-65-2824] of $SrRu_2O_6$ and the values reported in the paper[23]. The $Sr_{0.9}Ca_{0.1}Ru_2O_6$ XRD data is indexed with $SrRu_2O_6$ peaks which have comparatively high intensity peaks whereas the RuO_2 peaks are mixed in the background noise [fig 3.3 (a)]. XRD graph of 30% doped sample $Sr_{0.7}Ca_{0.3}Ru_2O_6$ have the same peaks of $SrRu_2O_6$ which are shifted but have a broader shape [fig 3.3 (b)]. The peaks are broadened because the crystallites formed in this doping trial have much smaller size compared to 10% doping as confirmed in the SEM images[Figure 3.2]. We also observe the impurity peaks of RuO_2 have significant intensity. Hence Rietveld study is undertaken for $Sr_{0.9}Ca_{0.1}Ru_2O_6$, with less RuO_2 impurity and then compared with the parent compound $SrRu_2O_6$.

3.3 Rietveld analysis of Synchroton data

As stated in [sec 1.4.1] $SrRu_2O_6$ is an antiferromagnet with very high Neel temperature $T_N = 565K$. It is also layered compound stacked along the c-axis. Previous studies of Rietveld analysis of the Neutron data on this compound gave a detailed description of the change of lattice parameters with temperature [25]. They observed that lattice parameter a remains relatively constant with temperature while the parameter c

increases linearly with temperature, this change was characterized as magnetoelastic coupling of Ru ions.

In this project, the synchrotron XRD data for $SrRu_2O_6$ and 10% doped form $Sr_{0.9}Ca_{0.1}Ru_2O_6$ is collected in the Temperature range 100K-400K, and analyzed with Rietveld fitting. Multiple phase refinement procedure is followed as the synchrotron data also contains RuO_2 peaks. Fullprof software was used to fit the data. The atomic structure is refined using the expected Hexagonal $P\bar{3}1m$ space group for $SrRu_2O_6$ and Tetragonal $P4_2/mnm$ for RuO_2 impurity. For the process of refinement, the parameters were refined in a particular stepwise process.The sequence followed for the refinement parameters is as follows the [(i) scale factor, (ii)The zero error, (iii) a, b, c parameters together (iv) u,v,w parameters independently 5) Preferred Orientation function parameters Eta, χ [34]. In XRD, the background can have its origin from diffraction of non-characteristic emissions of the X-ray tube, air scattering, sample fluorescence, over-illumination of the sample and many other factors. The experimental XRD pattern is, therefore, a contribution coming from the sample (i.e. diffraction) plus the background. That is the reason why we observe intensity even for 2θ values which are not a Bragg peak. The background here is fitted with a linear interpolation method.
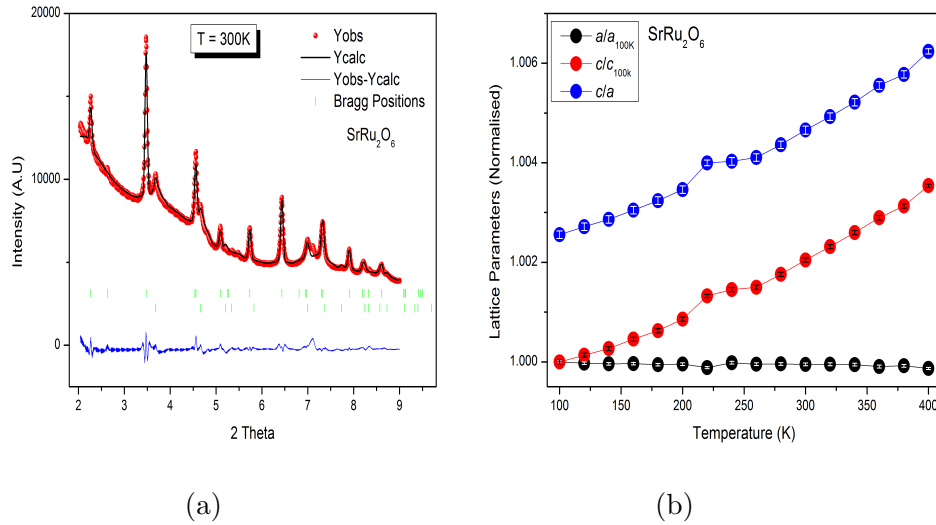

(a)   (b)

Figure 3.4: (a)Rietveld fit at 300k (b) Change in Lattice parameters with temperature for $SrRu_2O_6$, the spheres representing the data points contain error bars within them.

The Rietveld fit for $SrRu_2O_6$ at 300 K is shown in the [fig 3.4 (a)]. The goodness of fit χ^2 value for this fitting is 3.214. Similarly the fitting procedure is followed for all other temperatures and the refined parameters a,b,c are plotted normalised with the lowest temperature values. The graph of lattice parameters a/a_{100K} and c/c_{100K} and c/a for $SrRu_2O_6$ is shown in the [figure 3.4 (b)]. As seen from the graph, c/a and c/c_{100K} shows monotonous increase in values with temperature while a/a_{100K} shows non monotonous decrease in values. This shows there is a thermal expansion along the c-axis but the a-axis is almost constant with increasing temperature. It can be inferred from this that there is relatively less thermal expansion in the intra plane layers containing RuO_6 octahedra. However, the alternating layers of Sr cations are expanding along the c-axis. We observe a slight hump in c/a trend at 225K which is also observed in the general trend of c and a. The reason for this anomaly is presently not clear and the reason has to be further investigated.

Table 3.3: The statistical factors of the Rietveld fitting at different temperatures for the compound $SrRu_2O_6$

Temperature(K)	χ^2	$R_{wp}(\%)$	$R_{exp}(\%)$	$R_p(\%)$	$a/(\text{Å})$	$c/(\text{Å})$
100	2.38	17.1	11.09	33.1	5.20573	5.21903
120	2.36	16.9	11.04	32.8	5.20559	5.21973
140	2.35	17	11.09	32.8	5.20552	5.22042
160	2.40	17.2	11.09	33.3	5.20554	5.22141
180	2.39	17.2	11.10	33.4	5.20543	5.22229
200	2.41	17.3	11.12	33.4	5.20549	5.22351
220	1.79	15.0	11.19	30	5.20513	5.22594
240	2.36	16.7	11.20	33.4	5.20564	5.2266
260	2.41	17.5	11.27	34.3	5.20548	5.22685
280	2.36	17.4	11.27	33.7	5.20551	5.22821
300	3.214	20.9	11.7	43.6	5.20546	5.2297
320	2.38	17.5	11.35	33.9	5.20548	5.23112
340	2.36	17.6	11.45	34.2	5.20544	5.23259
360	2.71	19	11.55	41.3	5.20524	5.23414
380	2.45	17.7	11.33	34.2	5.20532	5.23538
400	1.83	15.3	11.33	30.4	5.20503	5.2375

Rietveld fit for $Sr_{0.9}Ca_{0.1}Ru_2O_6$ at 300 K is shown in the [fig 3.5 (a)] . It has a χ^2 value of 4.71 . The graph of lattice parameters a/a_{100K} and c/c_{100K} and c/a for $Sr_{0.9}Ca_{0.1}Ru_2O_6$ is shown in the [fig 3.5 (b)]. Here we observe the trend of c/a and c/c_{100K} is increasing monotonously with temperature which is similar to what we
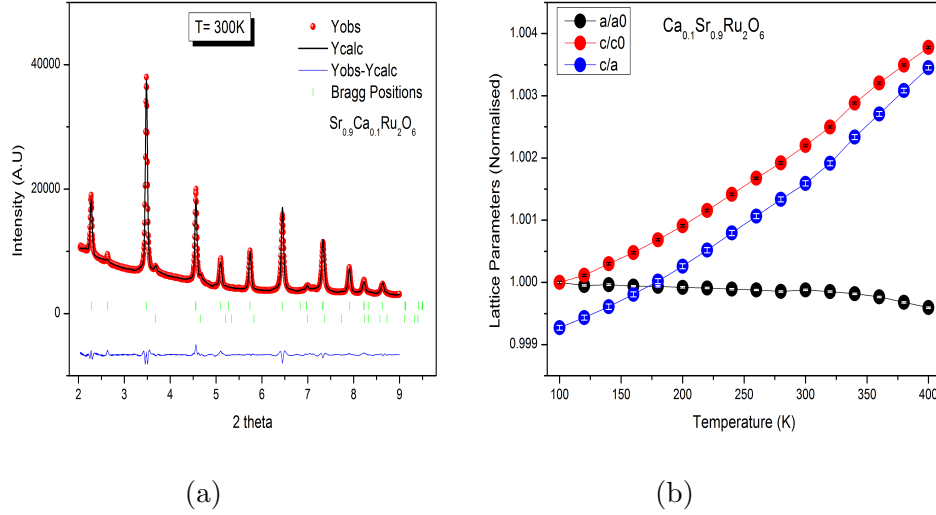
(a)   (b)

Figure 3.5: (a)Rietveld fit at 300 K (b) Change in Lattice parameters with temperature for $Sr_{0.9}Ca_{0.1}Ru_2O_6$, the spheres representing the data points contain error bars within them.

Table 3.4: The statistical factors and Lattice Parameters of the rietveld fitting at different temperatures for the compound $Sr_{0.9}Ca_{0.1}Ru_2O_6$

Temperature(K)	χ^2	$R_{wp}(\%)$	$R_{exp}(\%)$	$R_p(\%)$	$a/(\text{Å})$	$c/(\text{Å})$
100	4.04	8.87	4.39	11.9	5.20406	5.20027
120	4.36	9.40	4.50	12.9	5.2038	5.20086
140	4.27	10.2	4.44	14	5.20387	5.20183
160	4.5	9.32	4.39	12.4	5.20374	5.20275
180	4.48	9.36	4.42	12.4	5.20373	5.20383
200	4.78	9.64	4.41	12.8	5.20364	5.205
220	4.92	9.88	4.46	13	5.20359	5.20628
240	4.79	9.73	4.45	12.8	5.20349	5.20762
260	4.68	9.75	4.5	12.8	5.20343	5.20897
280	5.09	10.3	4.56	13.9	5.2033	5.21025
300	4.71	9.77	4.50	13	5.20343	5.21171
320	4.32	9.40	4.52	12.3	5.20329	5.21326
340	4.63	10.8	4.55	14.9	5.20311	5.21526
360	4.52	9.64	4.54	12.9	5.20285	5.21693
380	4.31	9.5	4.57	12.7	5.20239	5.21843
400	4.35	9.45	4.53	12.7	5.20195	5.2199

have observed in SrRu$_2$O$_6$. However the a/a_{100K} shows a decrease much higher than the pure compound.

In order to confirm this observation the change in lattice parameters for both the compounds is compared. The c parameter in both the compounds increases in a similar way which can be seen in the graph [Fig 3.6 (b)]. Suprisingly the lattice parameter a shows interesting feature which is clearly seen in the graph[Fig 3.6 a]. Here the lattice parameter a decreases much rapidly at room temperature for the doped compound. This suggests that the rate of expansion in the c-axis and the rate of compression for the a-axis for the structural unit cell is much higher for the doped compound compared to the pure compound. The possible reason for this observation is because the ionic radii of Ca is less than Sr, the rate of change is larger in doped ruthenate compared to the pure ruthenate. Hence we can say that there is a possible strain in the lattice of SrRu$_2$O$_6$ due to doping. However, no hump is observed in the c/a trend for Sr$_{0.9}$Ca$_{0.1}$Ru$_2$O$_6$ as observed in SrRu$_2$O$_6$, this can be clearly seen in the [fig 3.8] .All the three comparision graphs do not contain error bars as they are already mentioned in [fig 3.4 and 3.5]
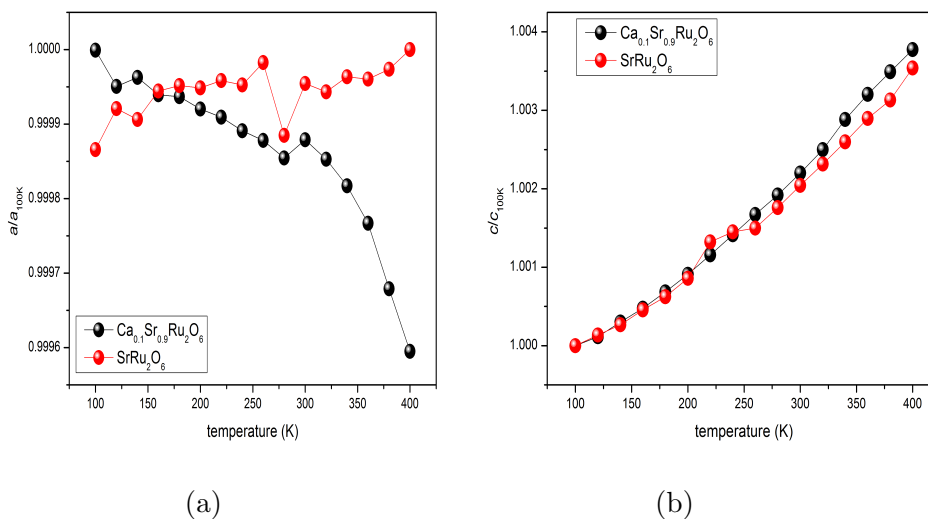

(a)   (b)

Figure 3.6: (a)Comparision of the lattice parameter a/a_{100K}, (b) and c/c_{100K} of SrRu$_2$O$_6$ and Sr$_{0.9}$Ca$_{0.1}$Ru$_2$O$_6$

Table 3.5: Refined structural Parameters for $SrRu_2O_6$ and $Sr_{0.9}Ca_{0.1}Ru_2O_6$ from Rietveld refinement of Powder Synchrotron diffraction data at T=300K

Refined Parameters	$SrRu_2O_6$	$Sr_{0.9}Ca_{0.1}Ru_2O_6$
a/ Å, b/ Å	5.20546	5.20343
c/Å	5.2297	5.211714
Scale factor	1.189×10^{-5}	3.749×10^{-5}
R_{exp}/%	11.7	4.50
R_{wp}/%	20.9	9.75
χ^2	3.214	4.718
Occupancy (Sr)	0.0833	0.7497
Occupancy (Ru)	0.16667	0.16667
Occupancy (O)	0.5	0.5
Occupancy (Ca)	-	0.00833

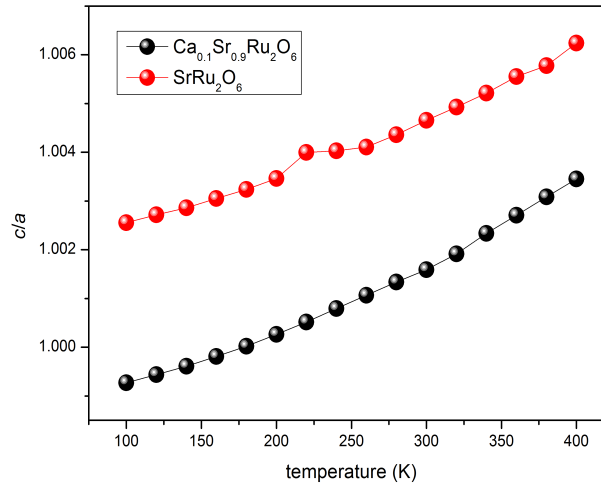

Figure 3.7: Comparision of c/a with temperature for $Sr_{0.9}Ca_{0.1}Ru_2O_6$ and $SrRu_2O_6$

3.4 Thermal Conductivity measurements

In this section we present the experimental data of thermal conductivity in bulk $SrRu_2O_6$ and its doped version $Sr_{0.9}Ca_{0.1}Ru_2O_6$.

Inorder to calculate Thermal conductivity of a material we have to understand how the thermal diffusivity is measured for a material. When we solve thermal conduction equation in one dimension for a body equation assuming an ideal case, we get the temperature response on the back side of the pellet

$$\Delta T = \Delta T_m [1 + 2 \sum_{n=1}^{\infty} (-1)^n \exp(\frac{(-n)^2 \pi^2 \alpha t}{L^2})] \tag{3.1}$$

where α is thermal diffusivity and L the thickness of the specimen and ΔT is the temperature rise of the specimen, ΔT_m is its maximum value, t is time after the pulse heating. The time when $\Delta T/\Delta T_m = \frac{1}{2}$ is the $t_{\frac{1}{2}}$ which is measured for each temperature. From $t_{\frac{1}{2}}$, we find the thermal diffusivity value using the relation ($\alpha = 0.1388\frac{L^2}{t_{\frac{1}{2}}}$) The specific heat of the compound is calculated using Dulong Petit law $c_p = \frac{3R}{M}$ where R is the universal gas constant and M is the molecular mass of the compound. Now, finally for measuring the thermal conductivity(κ) value we use the relation ($\kappa = \alpha c_p \rho$) where ρ is the density of the sample used which can be found out from the dimensions of the pellet used for measurement. Thermal Conducticty values for different temperatures is plotted for both the compounds and compared. It can be clearly seen from the graph in [fig 3.7] that above room temperature the doped compound $Sr_{0.9}Ca_{0.1}Ru_2O_6$ has increasing and higher thermal conductivity values compared to $SrRu_2O_6$. However more data points for $SrRu_2O_6$ will help to confirm this observation.

3.5 Resistance measurements

In order to compare the resitivity of parent and doped compound ,we performed both 4-probe and 2-probe electrical tranport measurements using PPMS instrument and LINKAM stage (THMS 600) respectvely. Low temperature two probe resistance
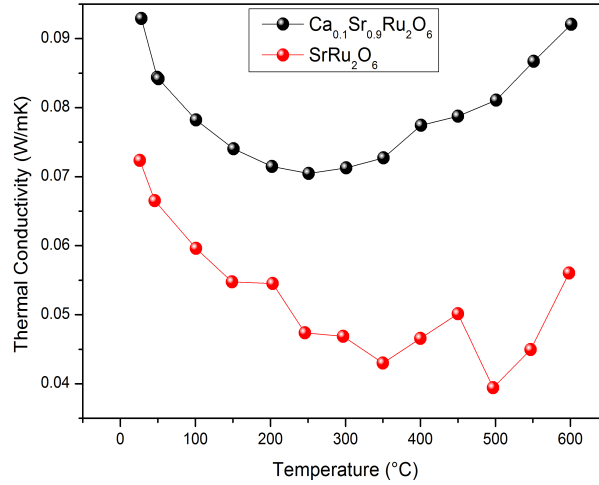
Figure 3.8: Variatons of thermal conductivity with temperature for $Sr_{0.9}Ca_{0.1}Ru_2O_6$ and $SrRu_2O_6$

measurements for both the samples is done using LINKAM stage in the temperature range (298K-128K). For this purpose, both the samples were first pelletised using the KBr press, in the form of a pellet of diameter 8mm and thickness 2 mm. The pellet was subsequently cut into a recatangular / elliptical shape. On these samples, contacts were made using silver paste. The wires connected with sample are covered with teflon tape to prevent shorting with the stage. These wires are connected to the leads of nano voltmeter (model 2450 SMU from Kiethley) for 2-probe measurements.

The graph[fig 3.9] depicts resistance values normalised at 128 K. In 2 probe, resistance values at 298K for $SrRu_2O_6$ is 6.276 ohms. Here the dimensions of the sample used is 3.35 mm length x 0.77mm width, x 0.69mm height rectanglar shaped pellet. Resistance values at 298K for $Sr_{0.9}Ca_{0.1}Ru_2O_6$ is 1.805 ohms and dimensions of the sample used is 3.95 mm length x 0.83mm width x 0.67mm height, ellipse shaped pellet. Resistivity is calculated for both the compounds at 298K using the dimensions of the pellet used in the experiment and resistance value at 298K. For $SrRu_2O_6$ we got a resitivity value of 0.995 x 10^{-3} Ohm-m at 298K which is close to the reported value of value of 2.33 x 10^{-3} Ohm-m [25]. For $Sr_{0.9}Ca_{0.1}Ru_2O_6$ we got a value of ≈ 0.254 x 10^{-3} Ohm-m at 298K. Resistance values for $SrRu_2O_6$ was also measured in PPMS instrument to get accurate 4-probe measurements of the sample in the temperature

range (300K-5K) which also shows semiconductor trend confirming 2-probe measurements. For $SrRu_2O_6$ We also found that $Ln(R)$ vs $1/T^{-4}$ following a linear trend with a slope of 23.14, intercept -4.47 for 4 probe measurement and a slope of 17.03, intercept -2.26 for 2-probe measurements in the temperature range (190K-298K).This might relate to Variable Range Hopping (VRH) . The activation energy for VRH can be estimated from the fitting and we plan to further repeat the measurements and from fitting parameters, we plan to determine the nature of conduction in parent compound.

Overall, the prime observation here is that the parent compound shows semiconducting like behaviour in this temperature range[25],whereas the doped version exhibits metal like resistivity. The linear increase in resistivity as a function of temperature in the doped compounds is more clearly seen in [figure 3.9 b]. This suggests that strain effects in the lattice parameter arising due to doping are significantly effecting the band structure and therefore the transport properties.
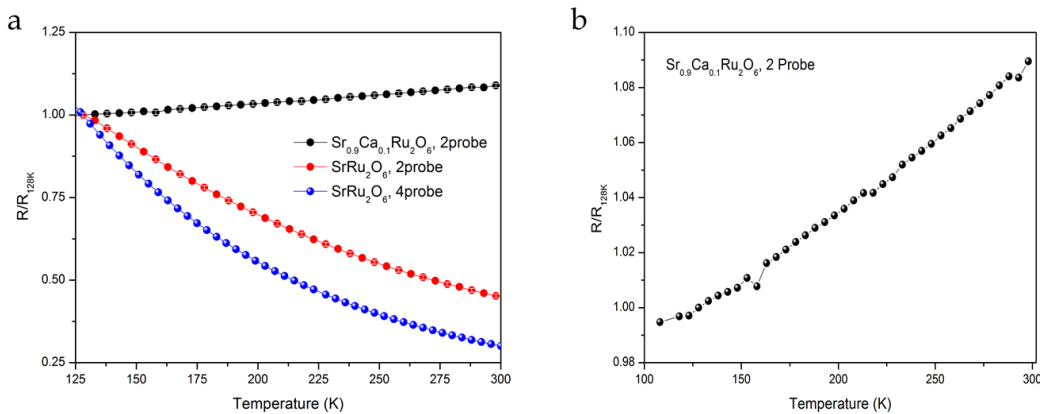

Figure 3.9: a)Comparision of Low temperature Resistance measurements for $SrRu_2O_6$ and $Sr_{0.9}Ca_{0.1}Ru_2O_6$ using 2-probe and 4-probe methods b) Resistance measurements for only $Sr_{0.9}Ca_{0.1}Ru_2O_6$ in the same temperature range

Chapter 4

Synthesis and Characterization of exfoliated nano sheets

As explained in [sec 1.2] layered TMO's are exfoliated for studying the electronic and magnetic properties which are starkly different from their bulk counterparts. However the layered TMO's are covalently bonded unlike the Graphene sheets which are stacked due to Van der Waals interaction. The TMO's in this study have weak inter-layer covalent bonding where as the intra-layer(in plane) covalent bonding is much stronger. Thus the magnetic oxides are exfoliated along the c axis. The exfoliated nanosheets also has applications in energy storage and nanoelectronic devices[9,10]. Hence large scale exfoliation is required to meet the purposes of the devices thus liquid exfoliation technique is employed.

4.1   Liquid exfoliation of oxide nanosheets

This technique requires a suitably selected solvent in which the layered metal oxide is introduced and the system is subjected to vibrations of ultrasonic frequencies using a sonication bath. An ion intercalant can be introduced into the system to stabilise the nano sheets thus produced. The vibrations by the sonic bath and the ion intercalation between the layers of the oxide stabilize the nano sheets produced [33].   For the

sonication process, the sample is kept for a long time (few hours) in the sonication bath. This increases the temperature of the sample which affects the way in which the layered TMO delaminates. The increased temperature probably causes a disordered exfoliation results. To avoid this, sonication bath is always maintained below the room temperature by using ice during the process of exfoliation. Finally, centrifugation arranges the nano sheets according to the density and then the supernatant containing the low density sheets are dropcasted onto Si substrate. The solvent used in the synthesis is ethanol and sonicator bath used for exfoliation is Sona pros PR-250 MP. For centrifugation Micro-200R 2405 centrifuge is used.

SNo	sample	weight mg	Ethanol ml	ion-intercalant	sonication time	Centrrifugation rate and time
1	Na_2IrO_3	17	100	LiOH	4 hrs	3000rpm 1hr
2	$RuCl_3$	12.2	50	none	4hrs	3000rpm 1hr
3	$SrRu_2O_6$	150	150	LiOH	4hrs	3000rpm 1hr
4	$Sr_{0.9}Ca_{0.1}Ru_2O_6$	50.5	50	none	3 hrs	3000rpm 2hrs

Table 4.1: Parameters followed in the liquid exfoliation of TMO's

4.2 Characterization of the exfoliated oxide nanosheets

In this section the charecterization of nano sheets is done using the standard microscopy techniques SEM, TEM and AFM required to charecterize any 2D nanosheets.

4.2.1 Na_2IrO_3 and $RuCl_3$

Na_2IrO_3 is a layered honeycomb structure and a candidate for Kitaev model. As a result this compound can exhibit Quantum spin liquid (QSL) sates, this can be observed experimentally using Raman spectroscopy[41]. $RuCl_3$ also shares similar honeycomb lattice structure but with a 4d metal ion. It is also a candidate for Kitaev model. Hence the Raman spectroscopy would give some Quantum spin liquid signatures[31]. In this project, the exfoliated nanosheets were just characterized by microscopy techniques.
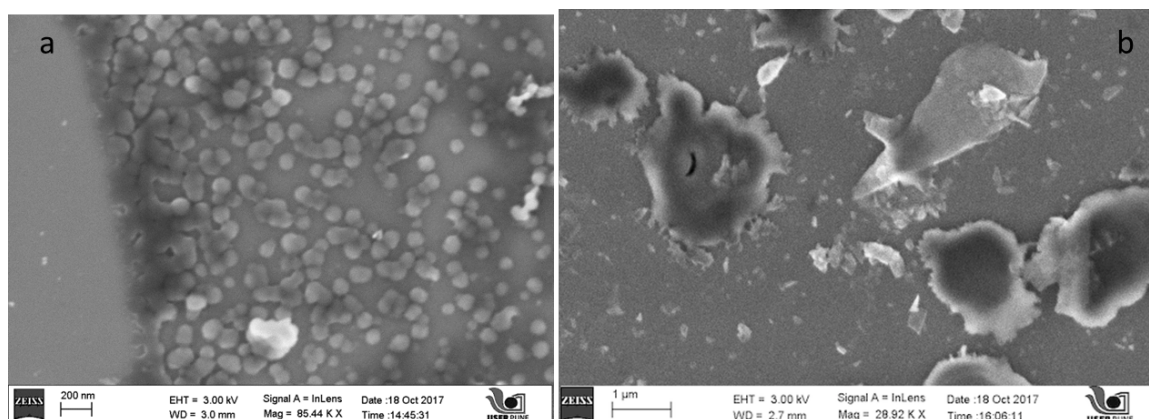
SEM images

Figure 4.1: a) SEM images of Na_2IrO_3 and b) $RuCl_3$

The SEM of the Na_2IrO_3 nanosheets is shown in the [figure 4.1 (a)]. It can be clearly seen that yield of nanosheets produced is large in number. We could also find some hexagonal sheets in the image as the sheets are produced by the delamination of the layered honeycomb crystal. The SEM image of $RuCl_3$ is seen in the [figure 4.1 (b)]. It shows relatively less number of nanosheets but with larger size.

AFM images

The AFM image of Na_2IrO_3 nanosheets is shown in the [figure 4.2 (a)]. We can clearly see a layered stack of flakes . In the [figure 4.2 (b)] the graph for height profile of this stack of images is shown. There is a rise in height of 2nm at uniform intervals along the line profile. This confirms that these are uniformly spaced nanosheets exfoliated from the bulk TMO. Na_2IrO_3 is known to be exfoliated along the c axis. The unit cell parameter c of the TMO is 1.0772 $\mathring{A}$ [28] . The AFM image of $RuCl_3$ nanosheets is observed in [figure 4.3 (a)] and its height profile in the [figure 4.3 (b)] which shows a height of 2nm . The unit cell parameter c for $RuCl_3$ is 0.60131 $\mathring{A}$ [29], so we may assume that image may contain few nanosheets which are not visible and are stacked under the observed nanosheet
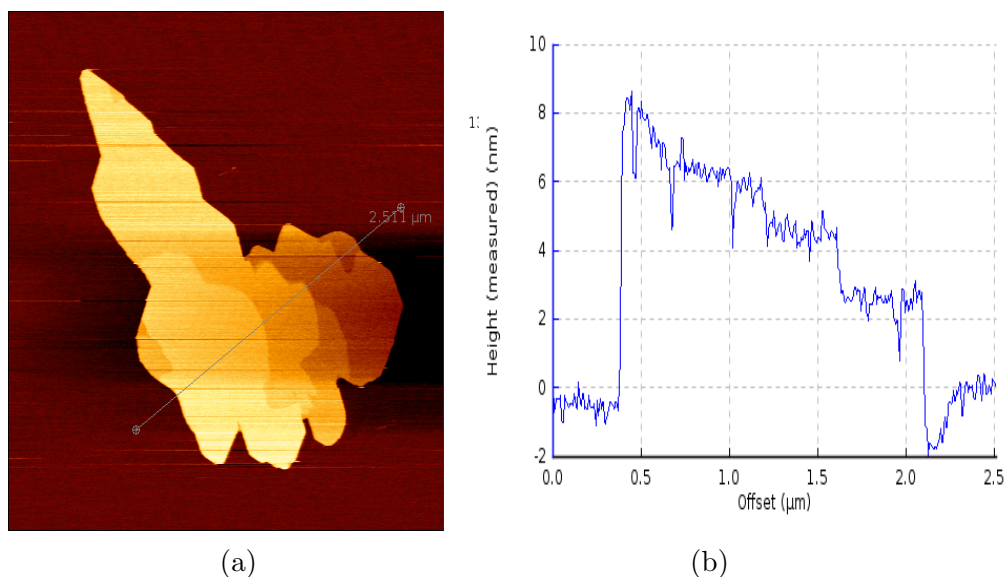
(a)

(b)

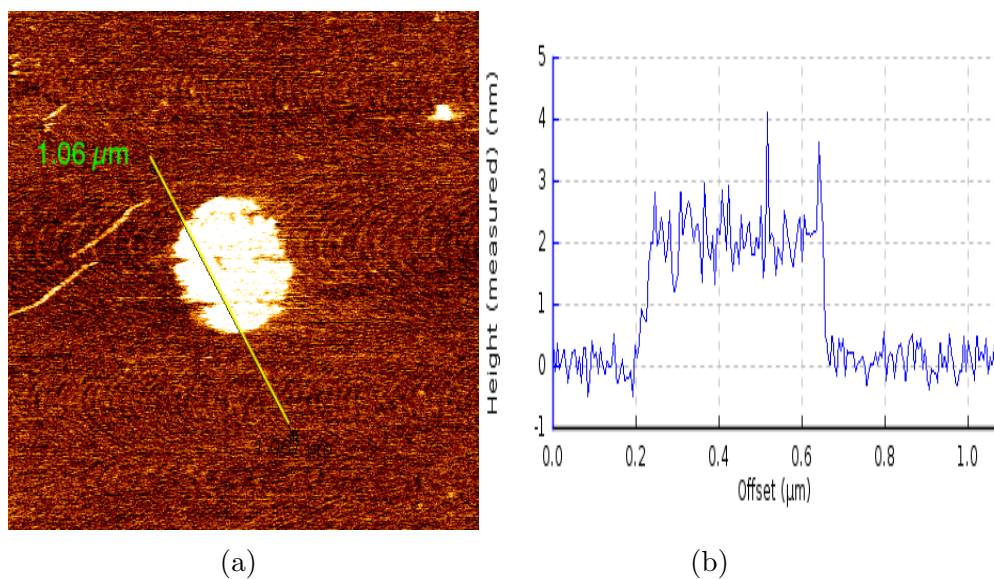Figure 4.2: (a)AFM image of Na_2IrO_3 nanosheets and (b) height profile for the image

(a)

(b)

Figure 4.3: (a)AFM image of $RuCl_3$ nanosheets and (b) height profile for the image

4.2.2 $Sr_{0.9}Ca_{0.1}Ru_2O_6$ and $SrRu_2O_6$

The comparision of the lattice parrameters with change in temperature gives information about how the unit cell is affected with temperature. The exfoliation of the layered structure into 2D form gives another approach to study the unit cell. This is because the neighbouring covalent bonding interaction is now reduced in 2D sheets.

Hence the antiferromagnet $SrRu_2O_6$ and its doped form $Sr_{0.9}Ca_{0.1}Ru_2O_6$ are again comparatively observed using the microscopy techniques.

SEM images

[Fig 4.4 a] shows the SEM images of $SrRu_2O_6$. It can be seen from the image that the yield of $SrRu_2O_6$ nanosheets produced is high and dispersed over a large surface area of the substrate. A hexagon shaped flake can be observed in the bottom part of the image. [Fig 4.4 b] shows sheets of $Sr_{0.9}Ca_{0.1}Ru_2O_6$ which are rather clustered into a group but there is a considerable amount of nanosheets which are distinctly shaped.

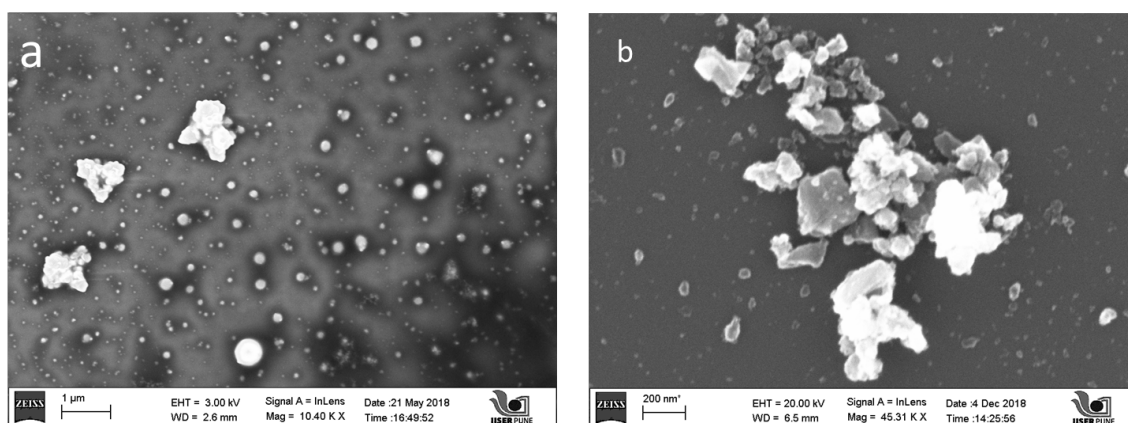Figure 4.4: a)SEM images of $SrRu_2O_6$ and b) $Sr_{0.9}Ca_{0.1}Ru_2O_6$

TEM images

HR-TEM gives the opportunity to observe atomic resolution of the nanosheets. Once we see atomic planes of the nanosheets the d-spacing of that particular (hkl) plane observed during imaging is calculated using Gatan microscopy software. We should use direct measurement of spacing using the raw file of the lattice image. For this, we measure 4-5 consecutive spacing and take an averge rather measuring a single spacing. From the Bragg's law [equation 2.1] we know the relation between 2θ and the corresponding d_{hkl} values. The measurement would be better if we first do the Fast Fourier Transform(FFT), then mask the point, and then take inverse FFT. It will give us clearer image of the lattice fringe. TEM image for $Sr_{0.9}Ca_{0.1}Ru_2O_6$ nanosheets is seen in the [fig 4.5].

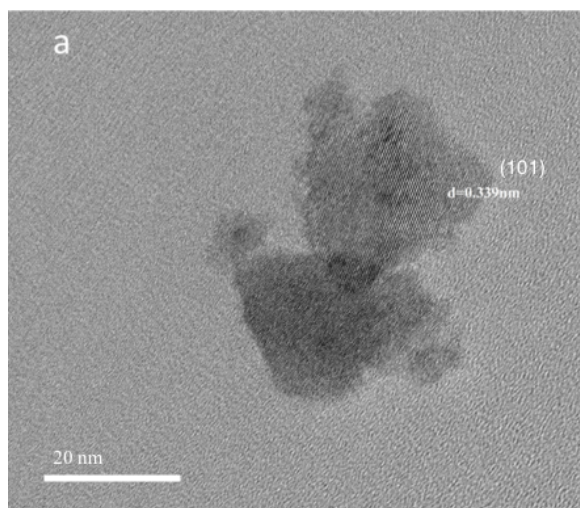Figure 4.5: HRTEM image of $Sr_{0.9}Ca_{0.1}Ru_2O_6$ with atomic resolution showing d-spacing of 3.4 Å corresponding to (101) plane
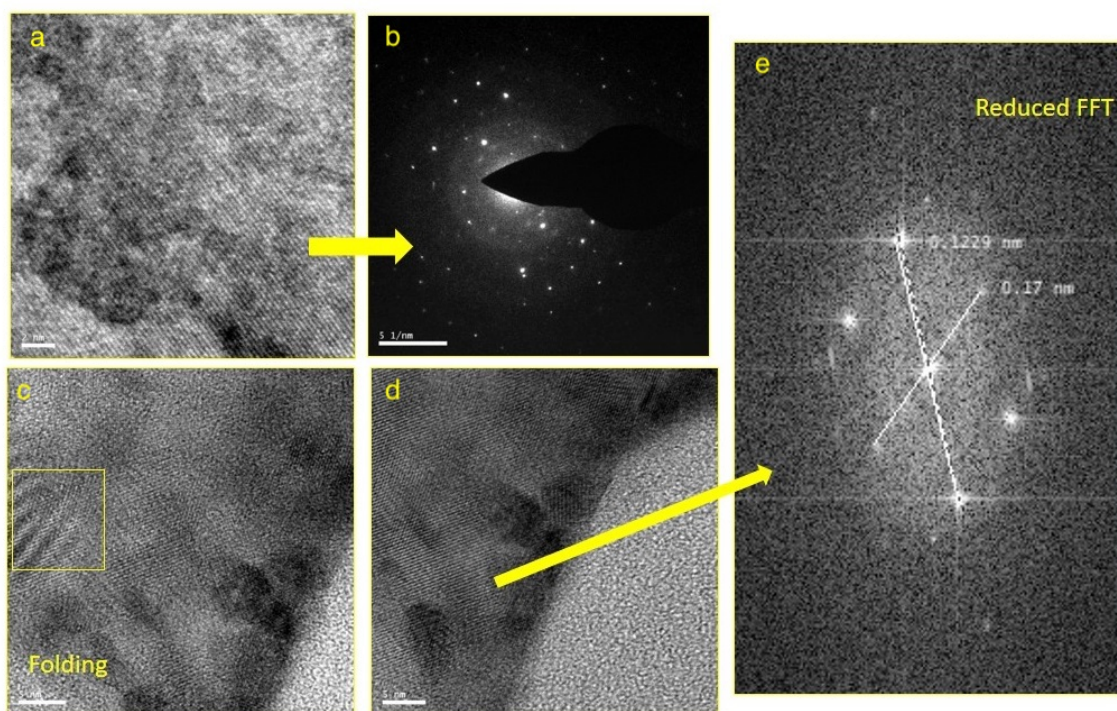

Figure 4.6: (a)HRTEM image of $SrRu_2O_6$ nano sheet (b)The electron diffraction pattern obtained on the same area. (c)shows another $SrRu_2O_6$ nanosheet with tendency for folding, highlighted by the yellow square. (d) & (e) shows the lattice spacing and the FFT (Fast Fourier Transform) image of the selected area , displaying hexagonal symmetry of the underlying lattice. [44]

We can see here the atomically thin layer with a d-spacing of 0.339 nm which corresponds to (101) plane which is the highest intensity peak indicated in the Lab XRD graph[Fig 3.3 a].

TEM image for $SrRu_2O_6$ is seen in the [fig 4.6]. Here we observe a nanosheet exhibiting crystalline nature of the atomically thin layers. For the same nanosheet diffraction pattern is also obtained. When the d-spacing between the planes is measured, we observed d=0.1229 nm corresponding to (-2 -1 3) plane and d=0.17nm corresponding to (2 0 2) plane. We also found a nanosheet which shows a tendency of folding. when the Fast Fourier Transform of an area of the image is done we could observe the hexagonal symmetry of the underlying lattice. [44]

AFM images

The AFM imaging for $Sr_{0.9}Ca_{0.1}Ru_2O_6$ is also done to extract information in the z-axis of the nanosheets, which is height of the nanosheets. The AFM mode used for this imaging is contact mode. As we can see in the [figure 4.7 a] there are two nanosheets along the line profile seen in the image. From the height profile shown in [figure 4.7 b] we find both the sheets are of 5nm height. This justifies that we are observing the nano sheets exfoliated from the bulk sample on the mica substrate.
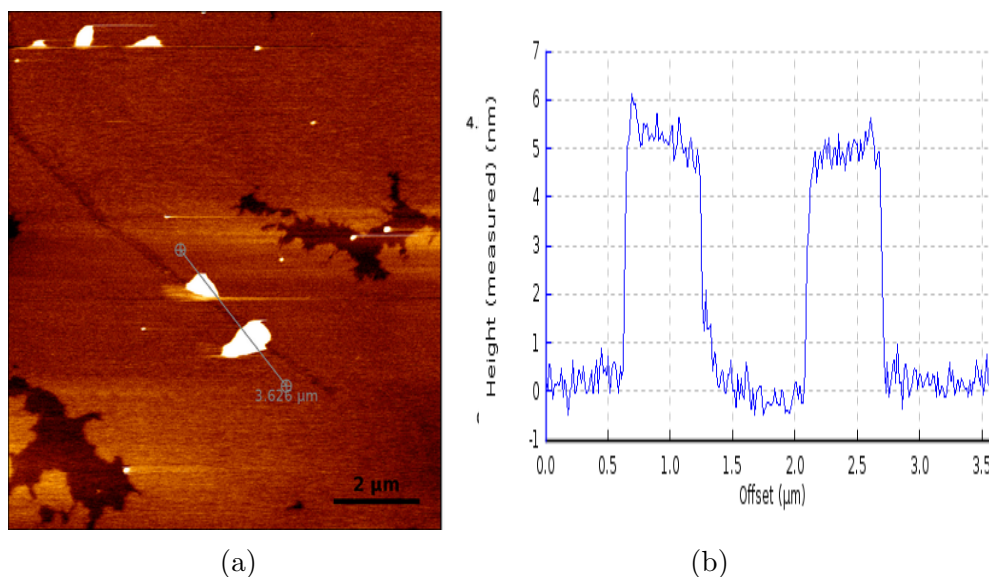

(a)   (b)

Figure 4.7: (a) AFM image of $Sr_{0.9}Ca_{0.1}Ru_2O_6$ nanosheets and (b) height profile for the image

Chapter 5

Summary and Future work

5.1   Summary

The 4d metal oxide $SrRu_2O_6$ is successfully doped with Calcium ions to form a new compound $Sr_{0.9}Ca_{0.1}Ru_2O_6$. The SEM images show hexagonal crystallites which have similar morphology compared to the parent compound $SrRu_2O_6$. XRD data confirms this as all the $SrRu_2O_6$ peaks have been observed with slight shift in the 2θ values. Rietveld analysis of the parent compound showed the temperature variation of the unit cell, which expands in the c axis . Rietveld analysis of the doped compound also showed this change along with an anomaly at room temperature for a parameter of $Sr_{0.9}Ca_{0.1}Ru_2O_6$. Thermal conductivity measurements of $Sr_{0.9}Ca_{0.1}Ru_2O_6$ also shows higher values above room temperature when compared with $SrRu_2O_6$. This can confirm the theoretical prediction of metallicity for $Sr_{0.9}Ca_{0.1}Ru_2O_6$ above room temperature. This doped TMO along with the 4d $RuCl_3$ and 5d oxide Na_2IrO_3 have been successfully exfoliated with the optimised parameters. The SEM images of the exfoliated 4d oxide nanosheets showed micron sized clumps as well as nanoscaled sheets, 5d oxide showed higher yield of nanosheets of size less than 2 nm. AFM images showed periodic spacing between a stack of nanosheets. The TEM images have showed atomic resolution of the nanosheets with the corresponding d-spacing.

5.2   Future work

Thermal conductivity measurements of the doped compound $Sr_{0.9}Ca_{0.1}Ru_2O_6$ should be supplemented with high temperature resistivity measurements. Also Seebeck Coefficient measurements of the sample enables us to calculate the Thermopower of the compound and explore the theoretical prediction of room temperature anomaly. For statistical significance, more data points should be taken for the thermal conductivity measurement of the parent compound $SrRu_2O_6$. Heat Capacity measurements and Transport measurements should be done for both the compounds. This gives a good comparative study of the 4d layered oxide and its doped form.

Further the exfoliated nanosheets should be further characterized with Raman spectroscopy and magnetic measurements. This may help in detecting the presence of topological driven states in these 4d and 5d oxide. Transport measurements can be done using AFM instrument for the layered nanosheets, which can be compared with the reported measurements in the bulk form.

Bibliography

1) C. N. R. Rao. Transition metal oxides. Annual Review of Physical Chemistry, 40(1):291326, 1989.

2) Gozar, A., et al. High-Temperature Interface Superconductivity between Metallic and Insulating Copper Oxides. Nature, vol. 455, no. 7214, 2008, pp. 782785., doi:10.1038/nature07293.

3) Kwon, Jang Yeon, and Jae Kyeong Jeong. Recent Progress in High Performance and Reliable n-Type Transition Metal Oxide-Based Thin Film Transistors. Semiconductor Science and Technology, vol. 30, no. 2, 2015, p. 024002., doi:10.1088/0268-1242/30/2/024002.

4) Cao, Gang, and Lance De-Long. Frontiers of 4d- and 5d-Transition Metal Oxides. 2011, doi:10.1142/8331.

5) Zheng, Haoping. Electronic Structure of CoO. Physica B: Condensed Matter, vol. 212, no. 2, 1995, pp. 125138., doi:10.1016/0921-4526(94)01100-f.

6) Kittel, C. Introduction to Solid State Physics. Wiley, 2005.

7) Maekawa, S., et al. Physics of Transition Metal Oxides. Springer, 2015.

8) Kaplan, Michael D., and George O. Zimmerman. Vibronic Interactions: Jahn-Teller Effect in Crystals and Molecules. Kluwer Academic, 2001.

9) Essler, Fabian H. L. The One-Dimensional Hubbard Model. Cambridge Univ.

Press, 2010.

10) Maria Hermanns, Itamar Kimchi, Johannes Knolle Physics of the Kitaev model: fractionalization, dynamical correlations, and material connections,4 May 2017.

11) Sasaki, Takayoshi, et al. Macromolecule-like Aspects for a Colloidal Suspension of an Exfoliated Titanate. Pairwise Association of Nanosheets and Dynamic Reassembling Process Initiated from It. Journal of the American Chemical Society, vol. 118, no. 35, 1996, pp. 83298335., doi:10.1021/ja960073b.

12) Sasaki, Takayoshi, and Mamoru Watanabe. Osmotic Swelling to Exfoliation. Exceptionally High Degrees of Hydration of a Layered Titanate. Journal of the American Chemical Society, vol. 120, no. 19, 1998, pp. 46824689., doi:10.1021/ja974262l.

13) Treacy, M. M. J., et al. Electron Microscopy Study of Delamination in Dispersions of the Perovskite-Related Layered Phases K[Ca2Nan-3NbnO3n-1]: Evidence for Single-Layer Formation. Chemistry of Materials, vol. 2, no. 3, 1990, pp. 279286., doi:10.1021/cm00009a018.

14) Schaak, Raymond E., and Thomas E. Mallouk. Prying Apart RuddlesdenPopper Phases: Exfoliation into Sheets and Nanotubes for Assembly of Perovskite Thin Films. Chemistry of Materials, vol. 12, no. 11, 2000, pp. 34273434., doi:10.1021/cm000495r.

15) Schaak, Raymond E., and Thomas E. Mallouk. Perovskites by Design: A Toolbox of Solid-State Reactions. Chemistry of Materials, vol. 14, no. 4, 2002, pp. 14551471., doi:10.1021/cm010689m.

16) Han, Yang-Su, et al. Exfoliation of Layered Perovskite, KCa2Nb3O10, into Colloidal Nanosheets by a Novel Chemical Process. Journal of Materials Chemistry, vol. 11, no. 4, 2001, pp. 12771282., doi:10.1039/b006045n.

17) Pei, Songfeng, and Hui-Ming Cheng. The Reduction of Graphene Oxide. Carbon, vol. 50, no. 9, 2012, pp. 32103228., doi:10.1016/j.carbon.2011.11.010.

18) Lee, C., et al. Measurement of the Elastic Properties and Intrinsic Strength of Monolayer Graphene. Science, vol. 321, no. 5887, 2008, pp. 385388., doi:10.1126/science.1157996.

19) Orlita, M., et al. Approaching the Dirac Point in High-Mobility Multilayer Epitaxial Graphene. Physical Review Letters, vol. 101, no. 26, 2008, doi:10.1103/physrevlett.101.267601.

20) Obraztsov, Alexander N. Making Graphene on a Large Scale. Nature Nanotechnology, vol. 4, no. 4, 2009, pp. 212213., doi:10.1038/nnano.2009.67.

21) Zhu, Yanwu, et al. Graphene and Graphene Oxide: Synthesis, Properties, and Applications. Advanced Materials, vol. 22, no. 35, 2010, pp. 39063924., doi:10.1002/adma.201001068.

22) Azadmanjiri, Jalal, et al. Two- and Three-Dimensional Graphene-Based Hybrid Composites for Advanced Energy Storage and Conversion Devices. Journal of Materials Chemistry A, vol. 6, no. 3, 2018, pp. 702734., doi:10.1039/c7ta08748a.

23) Hiley, Craig I., et al. Ruthenium(V) Oxides from Low-Temperature Hydrothermal Synthesis. Angewandte Chemie, vol. 126, no. 17, 2014, pp. 45124516., doi:10.1002/ange.201310110.

24) Wang, Da, et al. t2g-Orbital Model on a Honeycomb Lattice: Application to the antiferromagnetSrRu2O6. Physical Review B, vol. 92, no. 7, 2015, doi:10.1103/physrevb.92.075112.

25) Hiley, C. I., et al. Antiferromagnetism AtT¿500Kin the Layered Hexagonal ruthenateSrRu2O6. Physical Review B, vol. 92, no. 10, 2015, doi:10.1103/physrevb.92.104413.

26)Masayuki Ochi et al Phy Review B, 93,195149-2016

27) Agrapidis, Cli Efthimia, et al. Ordered States in the Kitaev-Heisenberg Model:

From 1D Chains to 2D Honeycomb. Scientific Reports, vol. 8, no. 1, 2018, doi:10.1038/s41598-018-19960-4.

28) Singh, Yogesh, and P. Gegenwart. Antiferromagnetic Mott Insulating State in Single Crystals of the Honeycomb Lattice materialNa2IrO3. Physical Review B, vol. 82, no. 6, 2010, doi:10.1103/physrevb.82.064412.

29) Plumb, K. W., et al. RuCl3: A Spin-Orbit Assisted Mott Insulator on a Honeycomb Lattice. Physical Review B, vol. 90, no. 4, 2014, doi:10.1103/physrevb.90.041112.

30) Simon Trebst, "Kitaev Materials". arXiv:1701.07056 [cond-mat.str-el].

31) Zhou, Boyi, et al. Possible Structural Transformation and Enhanced Magnetic Fluctuations in Exfoliated -RuCl 3. Journal of Physics and Chemistry of Solids, 2018, doi:10.1016/j.jpcs.2018.01.026.

33) Nicolosi, V., et al. Liquid Exfoliation of Layered Materials. Science, vol. 340, no. 6139, 2013, pp. 12264191226419., doi:10.1126/science.1226419.

34) Young, R. A. The Rietveld Method. Oxford University Press, 2002.

35) Byrappa, Kullaiah, and Masahiro Yoshimura. Handbook of Hydrothermal Technology. Elsevier, 2013.

36) Zhu, Fu-Yun, et al. 3D Nanostructure Reconstruction Based on the SEM Imaging Principle, and Applications. Nanotechnology, vol. 25, no. 18, 2014, p. 185705., doi:10.1088/0957-4484/25/18/185705.

37) TEM URL http://www.soest.hawaii.edu/HIGP/Faculty/sksharma/GG711/GG711Lec15TEM.pdf.

38) AFM URL http://www.nanoscience.gatech.edu/zlwang/research/afm.html.

39) XRD Wikipedia.

40) Synchrotron XRD wikipedia.

41) Satyendra Nath Gupta et al 2016 Raman signatures of strong Kitaev exchange correlations in (Na1xLix)2IrO3: Experiments and theory.

42) Geim, A. K., and K. S. Novoselov. The Rise of Graphene. Nature Materials, vol. 6, no.3, 2007, pp. 183191., doi:10.1038/nmat1849.

43) Suvidya V. Holmkar, "Synthesis and Magneto-Transport measure- ments in Magnetoresistive core shell material and 2D magnetic oxides". MS-Thesis, 2017,IISER Pune.

44) Suvidyakumar Homkar, B Bharat Chand, Shatruhan Singh Rajput, Shivprasad Patil, Ruediger Klingeler, Sunil Nair, Ashna Bajpai, "Atomically thin sheets of the layered honeycomb magnet SrRu2O6 by liquid exfoliation.[manuscript under preparation][arXiv:1904.12326]

45) Toby, Brian H. R Factors in Rietveld Analysis: How Good Is Good Enough? Powder Diffraction, vol. 21, no. 01, 2006, pp. 6770., doi:10.1154/1.2179804.

46) LFA wikipedia.